The endocytic recycling compartment maintains cargo segregation acquired upon exit from the sorting endosome

Shuwei Xie[a], Kriti Bahl[a], James B. Reinecke[a], Gerald R. V. Hammond[b], Naava Naslavsky[a], and Steve Caplan[a]

[a]Department of Biochemistry and Molecular Biology and the Fred and Pamela Buffett Cancer Center, University of Nebraska Medical Center, Omaha, NE 68198-5870; [b]Department of Cell Biology, University of Pittsburgh School of Medicine, Pittsburgh, PA 15261

ABSTRACT **The endocytic recycling compartment (ERC) is a series of perinuclear tubular and vesicular membranes that regulates recycling to the plasma membrane. Despite evidence that cargo is sorted at the early/sorting endosome (SE), whether cargo mixes downstream at the ERC or remains segregated is an unanswered question. Here we use three-dimensional (3D) structured illumination microscopy and dual-channel and 3D direct stochastic optical reconstruction microscopy (dSTORM) to obtain new information about ERC morphology and cargo segregation. We show that cargo internalized either via clathrin-mediated endocytosis (CME) or independently of clathrin (CIE) remains segregated in the ERC, likely on distinct carriers. This suggests that no further sorting occurs upon cargo exit from SE. Moreover, 3D dSTORM data support a model in which some but not all ERC vesicles are tethered by contiguous "membrane bridges." Furthermore, tubular recycling endosomes preferentially traffic CIE cargo and may originate from SE membranes. These findings support a significantly altered model for endocytic recycling in mammalian cells in which sorting occurs in peripheral endosomes and segregation is maintained at the ERC.**

Monitoring Editor
Jennifer Lippincott-Schwartz
National Institutes of Health

Received: Jul 20, 2015
Revised: Oct 19, 2015
Accepted: Oct 23, 2015

INTRODUCTION

The plasma membrane (PM) of mammalian cells is a highly dynamic compartment that continuously samples the environment and internalizes receptors and membrane lipids. Generally, internalization occurs via two major routes: 1) cargoes with specific signals in their cytoplasmic tails, including transferrin receptor (TfR) and low-density-lipoprotein receptor (LDLR), enter the cell through clathrin-mediated endocytosis (CME; Kirchhausen *et al.*, 2014), and 2) cargoes such as CD59 and β1-integrin are internalized via clathrin-independent endocytosis (CIE; Sandvig *et al.*, 2008). Regardless of their entry mechanism, endosomes carrying cargoes from both CME and CIE usually fuse with early/sorting endosomes (SEs) after their internalization (Naslavsky *et al.*, 2003). In SEs, the fate of cargoes is determined by either sorting to lysosomes for degradation or trafficking through the recycling pathway and return of cargo to the PM (Jovic *et al.*, 2010). To maintain the required balance of these molecules at the cell surface, recycling of the internalized molecules is a tightly regulated process. Aside from PM homeostasis, cell shape, and receptor retrieval, endocytic recycling is also key for a variety of cellular processes, including furrow cleavage and cytokinesis (Skop *et al.*, 2001; Montagnac *et al.*, 2008), cell migration (Caswell and Norman, 2008), and even polarity (Wang *et al.*, 2000).

Simplistically, recycling pathways have been described as either "fast recycling" or "slow recycling," depending on whether the recycling cargo is returned to the PM directly from SEs or is first transported to an additional organelle known as the endocytic recycling compartment (ERC), which is often localized near the microtubule-organizing center (MTOC) at the perinuclear region of the cell (Grant and Donaldson, 2009). Whereas the fast recycling route returns

This article was published online ahead of print in MBoC in Press (http://www.molbiolcell.org/cgi/doi/10.1091/mbc.E15-07-0514) on October 28, 2015.

The authors declare that they have no conflict of interest.

Address correspondence to: Steve Caplan (scaplan@unmc.edu).

Abbreviations used: CIE, clathrin-independent endocytosis; CME, clathrin-mediated endocytosis; 2D, two-dimensional; 3D, three-dimensional; dSTORM, direct stochastic optical reconstruction microscopy; EM, electron microscopy; ERC, endocytic recycling compartment; LDLR, low-density-lipoprotein receptor; MICAL-L1, molecules interacting with Cas-like1; MTOC, microtubule-organizing center; NA, numerical aperture; PA, phosphatidic acid; PBS, phosphate-buffered saline; PM, plasma membrane; RE, recycling endosome; SE, early/sorting endosome; SIM, structured illumination microscopy; TfR, transferrin receptor; TRE, tubular recycling endosomes; WGA, wheat germ agglutinin.

glycosphingolipids to the PM and is regulated by Rab4 (van der Sluijs *et al.*, 1992; Choudhury *et al.*, 2004), many receptors recycle via a Rab11-mediated pathway that traverses the ERC (Ren *et al.*, 1998).

Despite the significance of the ERC, surprisingly little is known about its composition and structure and the mode by which this organelle functions. It has been described as a group of tubular and vesicular membrane–bound structures that often condense around the MTOC (Maxfield and McGraw, 2004) and are likely connected by an elaborate network of tubular cisternae (Hopkins, 1983). Although resolution of the precise three-dimensional (3D) nature of the ERC will ultimately require complex cryo–electron microscopy (EM) and tomography, it is a crucial unanswered question whether cargo internalized via distinct pathways merges at the ERC or remains segregated in distinct regions or subcompartments within the ERC. Indeed, this question has important biological ramifications; previous studies pointed to the possibility of different cargoes returning to the PM via separate pathways (Mayor *et al.*, 2014), suggesting an active mechanism(s) to maintain segregation of cargo postsorting at the SEs.

Understanding the composition and function of the ERC has been further complicated in recent years by the plethora of membrane-bound tubular recycling endosomes (TREs) that have been identified (Naslavsky and Caplan, 2011). TREs are defined as tubular endosomes with lengths of up to 10 µm and diameters of up to 200 nm. We previously showed that the biogenesis of these structures occurs by a mechanism that includes the in situ generation of phosphatidic acid (PA) on membranes (Xie *et al.*, 2014), which helps to recruit both molecules interacting with CasL-like1 (MICAL-L1) and syndapin2 to the endosomal membrane and facilitates the bending of these structures by the syndapin2 F-BAR domain to form TREs (Giridharan *et al.*, 2013). However, whereas the mechanism of TRE biogenesis has been addressed, key questions regarding TRE function are unresolved. For example, although there is evidence of TREs regulating the transport of receptors from the perinuclear ERC back to the PM ("outgoing cargo"; Radhakrishna and Donaldson, 1997; Caplan *et al.*, 2002; Sharma *et al.*, 2009; Giridharan *et al.*, 2013), it is unclear whether TREs *also* transport cargo from SEs to the ERC ("incoming cargo"). In addition, the relationship between the "classical" Rab11a tubulovesicular endosomes (at or near the ERC) and MICAL-L1–containing TREs is poorly understood. In particular, it is unclear whether Rab11a endosomes and TRE transport distinct or overlapping cargo.

In this study, we used superresolution microscopy to address the composition, morphology, and structure of the ERC at subdiffraction resolution. Using structured illumination microscopy (SIM) and dual-channel two-dimensional (2D) direct stochastic optical reconstruction microscopy (dSTORM), as well as 3D dSTORM, we obtained new information about ERC morphology and cargo segregation. We show that CME and CIE cargo remain segregated at the ERC, suggesting that after exit from the SE, additional sorting may not occur. In addition, SIM and 3D dSTORM data support the notion that some but not all ERC vesicles are tethered by contiguous "membrane bridges." Finally, we demonstrate that TREs preferentially facilitate CIE cargo trafficking and that some TREs originate from SE membranes rather than from the ERC. Overall our study supports a model for endocytic recycling in which sorting occurs in peripheral endosomes and segregation is maintained at the ERC.

RESULTS

Despite considerable advances in understanding internalization and early endocytic events, the nature and the function of the ERC remain incompletely understood. Although a multitude of studies have addressed the differential internalization requirements for receptors that traffic via CME as compared with CIE, whether these cargoes undergo mixing at the ERC or remain segregated throughout their recycling itineraries has yet to be determined.

The ERC is typically considered to be a highly complex series of vesicles and tubules concentrated at the perinuclear area. However, given the lack of cryo-EM tomography or superresolution data, the precise nature of the ERC region is unknown. To address the nature and organization of the ERC, we applied superresolution SIM imaging and compared it with micrographs obtained by confocal microscopy (Figure 1). Whereas ~300-nm resolution by confocal microscopy images depict Rab11a (the ERC marker selected) in a compact perinuclear region (Figure 1A; yellow arrows), 3D SIM imaging at ~110-nm resolution suggests that although the Rab11a structures are indeed densely packed, many appear to be single, isolated vesicles, suggesting that the ERC may not be entirely enveloped by a single, contiguous membrane (Figure 1B and inset; see also Supplemental Movie S1). To ensure that membrane-contiguous organelles were not disrupted by our SIM fixation process, we costained for Rab11a and the Golgi marker GM130 and subjected the cells to SIM analysis. As demonstrated in Figure 1, C–E, and Supplemental Movie S2, the Golgi retained its typical contiguous, ribbon-like structure under these conditions, whereas Rab11a was mostly localized to vesicles as expected. These observations support the notion that the ERC may be a compartment that contains a complex combination of linked endosomal membranes and potentially independent structures.

Because Rab11a can segregate into microdomains of sorting endosomes (Sonnichsen *et al.*, 2000), we cannot rule out the possibility that "membrane bridges" (with or without Rab11a bound to the membrane) may connect individual membrane-bound vesicles in the recycling compartment. To help address this prospect, we applied 3D SIM imaging to cells that we pulsed and chased with labeled transferrin. We then monitored ERC-localized TfR and endogenous cellubrevin, a soluble *N*-ethylmaleimide–sensitive factor attachment protein receptor and marker of ERC membranes (Daro *et al.*, 1996). As demonstrated in Figure 2, A–C, although many TfR-containing endosomes appeared to be on distinct membranes, the 3D SIM imaging allowed us to frequently observe "membrane bridges" marked by cellubrevin (green) that linked TfR-containing endosomes (Figure 2, A–C; green arrows). In some cases, we detected structures containing both cellubrevin and TfR (Figure 2D, bottom left corner), whereas in other cases, TfR- and cellubrevin-containing structures clearly remained distinct from one another (Figure 2D, top half of micrograph). Cellubrevin "bridges" between transferrin-labeled membranes were as long as 400–500 nm in some cases (Figure 2E). To better resolve the potential linkage between apparently distinct endosomal structures within the ERC, we turned to 3D dSTORM imaging. 3D dSTORM displayed a dramatic increase in resolution compared with standard epifluorescence (compare Figure 2, G with F). Although the ~60 nm lateral *x*/*y* precision (88-nm Nyquist resolution) obtained with 3D dSTORM (Figure 2H) did not approach the resolution that we typically achieved for 2D dSTORM (see later discussion of Figures 4 and 7), the 3D imaging allowed us to identify connections of up to 500 nm between Rab11a-containing endosomes at the ERC (Figure 2G(1)). On the other hand, other Rab11a-containing clusters of endosomes within the ERC appeared to be independent of one another (Figure 2G(2)), suggesting the possibility that parts of the ERC maintain an underlying connection, whereas others do not.

Given the complexity of the ERC, we next asked whether cargo internalized via CME and CIE would both localize to the same Rab11a-containing regions of this compartment. To address this question, we

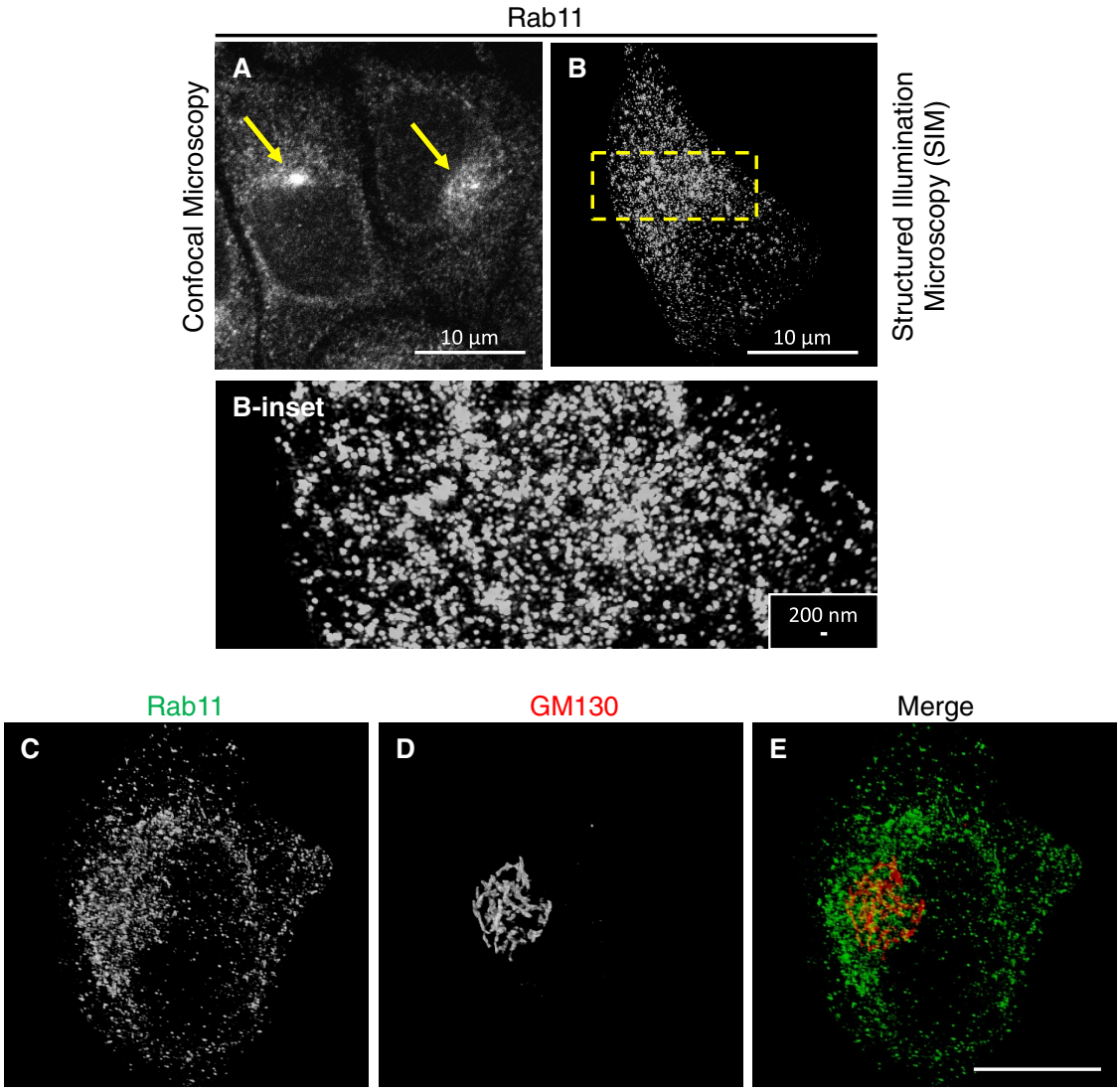

FIGURE 1: The 3D SIM characterization of Rab11a recycling endosomes in the ERC. (A, B) Rab11a-labeled recycling endosomes were immunostained with anti-Rab11a and Alexa 488–conjugated anti-rabbit secondary antibody and visualized by confocal microscopy (A) and SIM (B). Yellow arrows point to the dense perinuclear area (A). The dashed rectangle in the SIM micrograph (B) is shown enlarged in the inset. (C–E) HeLa cells were stained with anti-Rab11a and anti-GM130 together with the corresponding secondary antibodies and imaged by SIM. Scale bar, 10 µm.

followed TfR and CD59, a glycosylphosphatidylinositol-anchored protein transported via EHD1- and MICAL-L1–containing TREs (Cai *et al.*, 2011). As demonstrated by high-resolution SIM imaging, TfR displayed a high level of overlap with Rab11a (Figure 3, A–C and insets, and Supplemental Movie S3). To monitor CD59 at the ERC, we incubated cells with anti-CD59 antibody for 30 min. We then stripped noninternalized antibody from receptors still at the cell surface, and chased the internalized CD59–antibody complex for 2 h to allow it to reach the ERC. Although standard confocal microscopy micrographs suggest some potential overlap between CD59 and Rab11a (Figure 3, D–F), higher-resolution SIM images (Figure 3, G–I and insets, and Supplemental Movie S4) depict only limited colocalization.

On the basis of these experiments showing that TfR but not CD59 displays considerable overlap with Rab11a at the ERC, we next predicted that cargo internalized either via CME (i.e., TfR) or CIE (i.e., CD59) would remain segregated after being trafficked to the ERC. To test this, we cointernalized transferrin and anti-CD59 antibody for 30 min (pulse) to examine peripheral SEs or for 30 min followed by a 30-min chase into the ERC and subjected the cells to SIM analysis (Figure 4, A–C) or dSTORM (Figure 4, D and E, and Supplemental Figures S1 and S2). SIM analysis partially resolved the CD59 and TfR after chase into the dense ERC region (Figure 4, A–C and insets). In particular, rotation of the 3D images along the *y*-axis shows that CD59- and TfR-containing structures are either mostly distinct or at least well segregated (Supplemental Movie S5). dSTORM imaging at ~10-nm precision and 33- to 39-nm Nyquist resolution further supported the SIM data, showing that CD59 and TfR were mostly segregated within the ERC (Figure 4E and Supplemental Figure S2). dSTORM imaging in the periphery of cells that had taken up both cargoes for 30 min also yielded very limited colocalization of TfR and CD59 (Figure 4D and Supplemental Figure S1), although areas of overlap could be discerned (see arrows). Although we cannot rule out the possibility that these are distinct compartments that have not been clearly resolved in the *z*-axis, they most likely represent microdomains of peripheral SEs displaying ongoing sorting.

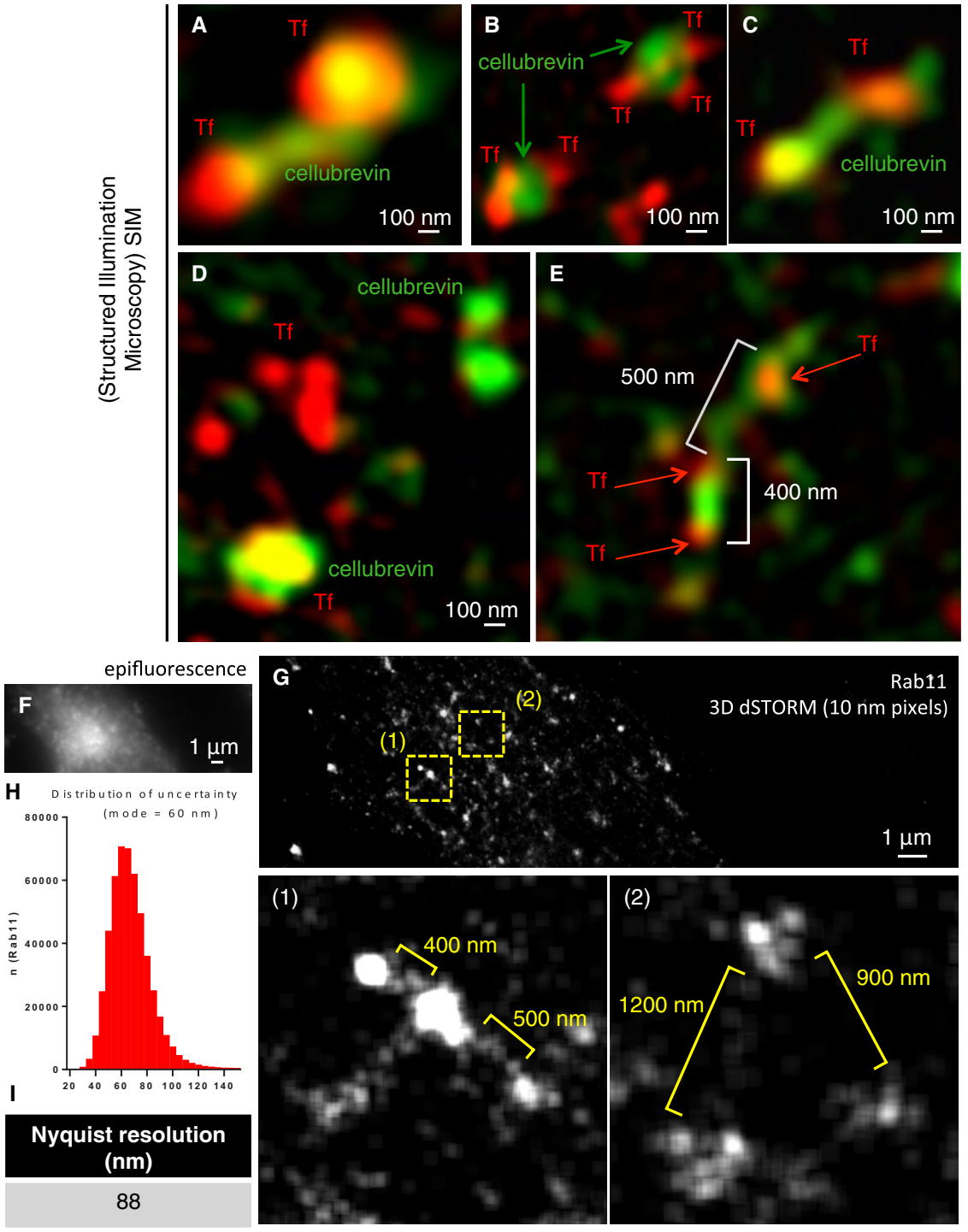

FIGURE 2: Linkage between recycling endosomes in the ERC via "membrane bridges" as observed by SIM and 3D dSTORM imaging. (A–E) HeLa cells on coverslips were transiently transfected with GFP-cellubrevin for 18 h, serum starved for 1 h, and then allowed to internalize Alexa 568–conjugated transferrin for 15 min at 37°C, followed by a 15-min incubation in fresh medium before fixation. The sample was subjected to SIM imaging. (F–H) Endogenous Rab11a in the perinuclear area is depicted by epifluorescence microscopy (F) or a reconstructed 3D dSTORM image (G). HeLa cells plated on glass-bottom MatTek dishes were fixed and stained with anti-Rab11a antibody, followed by Alexa 647–conjugated anti-rabbit antibody. The 3D dSTORM was performed by acquiring >9 × 10^6 localizations during 40,000 frames obtained every 50 ms. The single-molecule localizations were reconstructed into a normalized Gaussian image at 10-nm pixel size using the ThunderSTORM plug-in in ImageJ. Enlarged images of the dashed box areas in G are shown in (1) and (2). A histogram (H) representing the calculated uncertainty was plotted on frequency distribution graphs with 27 bins, and the mode of the distribution was taken as the lateral precision. (I) The Nyquist resolution.

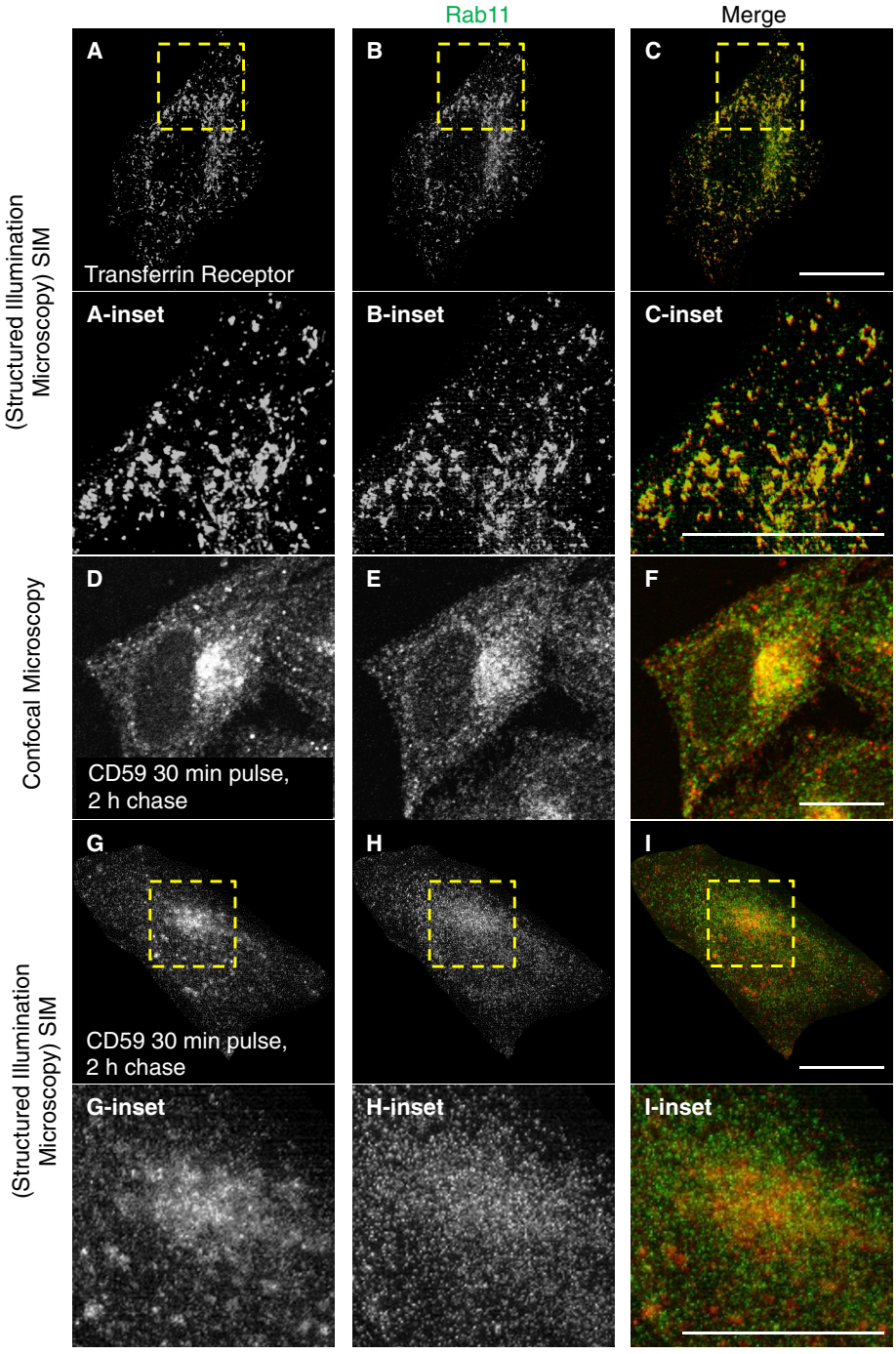

FIGURE 3: The CIE cargo CD59 is absent from perinuclear Rab11a recycling endosomes in the ERC. (A–C) HeLa cells were fixed and stained with anti-TfR and anti-Rab11a antibodies, along with corresponding secondary antibodies. The localization of TfR (A) and Rab11a recycling endosomes (B) was analyzed with SIM. Insets highlight the boxed area with higher magnification. Scale bar, 10 μm. (D–F) HeLa cells were incubated with anti-CD59 antibody for 30 min at 37°C, followed by an acid strip. The cells were then incubated in fresh medium for 2 h before fixation. CD59 was visualized with Alexa 568–conjugated anti-mouse antibody (D). Rab11a was visualized with rabbit anti-Rab11a antibody and Alexa 488–conjugated anti-rabbit antibody (E). Cells were imaged by confocal microscopy. Scale bar, 10 μm. (G–I) The same sample from D–F was subjected to SIM analysis. The dashed box denotes the perinuclear area. Insets exhibit the boxed area with higher magnification. Scale bars, 10 μm.

The significant segregation between CME and CIE cargoes at the ERC, along with the failure of the latter cargoes to localize to Rab11a-containing recycling endosomes (REs) raised the possibility of very limited post-SE sorting, as these two classes of cargoes remain separate throughout their recycling itinerary to the PM. To clarify the role of Rab11a in sorting of distinct cargo classes, we used the myosin Vb tail as a "surrogate" for Rab11a (Hales *et al.*, 2002). This truncated motor protein becomes trapped in the ERC, and, due to its coupling with Rab11a, cargoes that use the Rab11a-myosin Vb pathway are similarly coalesced in the ERC. As demonstrated, the CME cargoes TfR (Figure 5, A–C, green arrows) and LDLR (Figure 5, D–F, blue arrows) were retained in the ERC and highly colocalized with the myosin Vb tail (quantified in Figure 5M and with profile scans in Supplemental Figure S3, A and B). On the other hand, CIE cargo, such as CD59 (Figure 5, G–I, red arrows) and β1-integrin (see Figure 7, J–L, yellow arrows, later in the paper) displayed very limited localization to the myosin Vb tail structures (quantified in Figure 5M and profile scan in Supplemental Figure S3, C and D). Moreover, the myosin Vb tail did not interfere with TRE generation as discerned by MICAL-L1 or syndapin2 immunostaining (Supplemental Figure S3, E–J), both of which are required to facilitate TRE biogenesis and endocytic recycling (Giridharan *et al.*, 2013), although occasionally MICAL-L1 could also be observed in partial overlap with the myosin Vb tail. These data support the idea that MICAL-L1 acts independently of Rab11a in controlling endocytic recycling and that CME and CIE cargoes undergo distinct recycling pathways from their internalization and throughout their recycling itineraries.

To address further the seclusion of the clathrin-independent recycling pathway and its lack of reliance on Rab11a, we depleted Rab11a from cells (Figure 6A) and determined the degree to which TfR recycling is affected compared with the CIE cargoes CD59 and β1- integrin. As demonstrated, whereas reduced Rab11a expression severely impaired TfR recycling, no significant effect was measured for CD59 or β1-integrin (Figure 6, B and C). Moreover, overexpression of a dominant-negative Rab11 slowed the rate of TfR recycling without significantly affecting the rate of CD59 recycling (Figure 6, D and E). Overall these data are consistent with the notion that recycling CME and CIE cargoes are segregated within the ERC and that Rab11a regulates recycling of CME but not CIE cargoes.

TREs containing MICAL-L1 and Rab11a are partially concentrated in the ERC. A major unanswered question concerns the relationship between MICAL-L1-TRE and Rab11a-RE. On the basis of the segregation that we observed between CME and CIE cargoes and the select role of

Rab11a in regulating the recycling of CME cargoes, we hypothesized that Rab11a and MICAL-L1 may segregate within the ERC. As demonstrated by SIM imaging (Figure 7, A–C, and Supplemental Movie S6), despite the localization of the distal TRE tips to the dense ERC, the TREs show no appreciable overlap with Rab11a. Because SIM is limited to ~100-nm resolution, we turned to study the ERC at higher resolution, using two-channel dSTORM to image cells costained for endogenous Rab11a and MICAL-L1 (Figure 7D and Supplemental Figure S4). Two areas of the cell were enlarged in Figure 7D; Figure 7Da represents a TRE in the midst of the dense Rab11a ERC, whereas Figure 7Db depicts a TRE from a more peripheral area of the cell. With calculated precision levels of 10 and 13 nm for MICAL-L1 and 18 and 16 nm for Rab11a in Figure 7D, a and b, respectively, and Nyquist resolution of 31–48 nm (Supplemental Figure S4), we observed minimal colocalization between Rab11a and MICAL-L1 both at the ERC and in the periphery. These data support our model in which the ERC maintains segregation of resident proteins and cargoes.

Previous studies support a role for TREs in regulating cargo transport from the ERC to the PM (Caplan *et al.*, 2002; reviewed in Maldonado-Baez *et al.*, 2013). Establishing whether TREs might also carry cargo *from* the SE *to* the ERC has been a difficult question to address (Figure 8A). We previously showed that phospholipase D (PLD) inhibitors (which prevent PA generation) induce the loss of TRE (Figure 8, B and C; Giridharan *et al.*, 2013). To determine the membrane origin of TREs, we developed an assay in which washout of the PLD inhibitors led to synchronized de novo TRE generation ("burst") beginning within 20 min (Figure 8D) and reaching a peak at 1 h after inhibitor removal (Figure 8E). Using this assay, we costained cells undergoing TRE regeneration 20 min after washout with markers for the ERC and SEs. As demonstrated (Figure 8, F–H), the SE marker Rabenosyn-5 could be detected on punctae at the apex of TREs (see inset; arrows) and along TRE membranes, and this colocalization was also observed in untreated cells (Supplemental Figure S5, A–C, and insets). However, other markers for SE, such as Rab5 and EEA1, were not observed, suggesting that TREs are derived from a select subset of SEs (unpublished observations). Moreover, surface-stained wheat germ agglutinin (WGA) internalized for 5 min did not appear in MICAL-L1–containing TREs, indicating that these TREs are not derived from the PM (Supplemental Figure S6). In addition, we observed that newly generated TREs localize to the periphery and are typically absent from the ERC. Overall these data lead us to suggest that some TREs originate from a subset of SEs containing Rabenosyn-5, and likely transport cargo from SEs to the ERC.

Our next goal was to determine which cargoes might potentially be transported along peripheral TREs to the ERC. To address cargo selectivity in TRE, we initially examined the carriers that transport the CIE cargo CD59. As depicted by SIM micrographs in Figure 9, A–C, CD59 internalized for 9 min clearly localized to MICAL-L1-TRE. On the other hand, TfR internalized via CME was absent from MICAL-L1-TRE after either 3 min (Figure 9, D–F) or 9 min of internalization (Supplemental Figure S7, A–C, and insets). We next analyzed cargo selectivity on newly generated TREs derived from Rabenosyn-5–containing SEs. To this aim, we treated cells for 30 min with PLD inhibitors, followed by a 20-min washout in complete media, to allow generation of MICAL-L1–containing TREs. In the last 10 min of washout, we monitored internalized cargo. As demonstrated (Figure 9, G–J), internalized CD59 was sorted into newly formed Rabenosyn-5– and MICAL-L1–containing TREs (quantified in Supplemental Figure S7, D and E). In contrast, whereas TfR was detected in partial overlap with Rabenosyn-5 at SEs (Figure 9, K–N; yellow arrow), it was entirely absent from the TREs containing both MICAL-L1 and Rabenosyn-5 (Figure 9, K–N; quantified in Supplemental Figure S7, D and E). These data further support the notion that MICAL-L1-TREs preferentially mediate the transport of CIE cargo from SEs to the ERC.

To further support or negate the idea that TREs transport CD59 to the ERC from SEs, we carried out live-cell imaging experiments to follow CD59 trafficking along newly generated TREs (Figure 10). To this aim, we first incubated cells with PLD inhibitors to disrupt TREs. We then washed out the inhibitors (leading to acute TRE biogenesis) and provided anti-CD59 to the cells so that CD59 could be internalized and monitored. At the initial time point imaged (Figure 10; 45 s), we observed little or no CD59 in the ERC (marked by a dashed yellow region of interest), and the TRE monitored had not yet undergone biogenesis and was not visible. At the 1:45 time point, no CD59 had yet reached the ERC (dashed yellow region of interest and blue arrow), but the MICAL-L1–marked TREs began to grow in the cell periphery (red arrow). At 2:45 and 3:45 time points, the TREs continued to grow from the periphery toward and into the ERC region, with some CD59 accumulating at the ERC. Finally, at the 4:45 time point, the newly generated TREs, marked by MICAL-L1 and CD59, were extended fully into the ERC (dashed yellow region of interest and blue arrow). Although the signal was weaker than that of MICAL-L1, CD59 partially colocalized with MICAL-L1 on the TREs and reached the ERC. These data strongly support the notion that, in addition to its characterized role in regulating ERC-to-PM trafficking, the source of some TRE membrane derives from peripheral SEs, and these TREs can transport CIE such as CD59 from SEs to the ERC.

DISCUSSION

Composition of the ERC

The long-standing paradigm for the ERC holds that it is situated in a perinuclear region of the cell adjacent to the MTOC and comprises a complex series of tubular-vesicular endosomes (Yamashiro *et al.*, 1984; Mayor *et al.*, 1993; Marsh *et al.*, 1995; Maxfield and McGraw, 2004). Distinguishing whether the ERC is enveloped mostly by a single contiguous membrane as originally proposed by Hopkins (1983) or is a region of mostly individual vesicles and tubules has been a difficult question to resolve. Although ultimately techniques that directly label membranes and allow 3D analysis (such as cryo-EM coupled with tomography) will help determine the nature of the ERC more precisely, the inherent fusion-fission dynamics of this organelle may complicate this endeavor. In this study, however, we took advantage of advanced superresolution and single-molecule imaging techniques to address cargo segregation within the ERC and the physical separation of cargo localized to ERC vesicles and TREs.

Given that a growing body of evidence, including our findings here, supports the idea that CME and CIE cargo sorting occurs at the SEs before transport to the ERC, it was rational to hypothesize that the cargoes *remain* segregated to either distinct ERC endosomes or membrane subdomains within the ERC until they are recycled back to the PM (see later discussion of the model presented in Figure 11). To address this question and circumvent the limitations of light microscopy in resolving distances less than ~300 nm, we used both SIM and dSTORM to reexamine the ERC organization and cargoes that recycle via this compartment. By these two superresolution techniques, with Rab11a and cellubrevin as ERC markers, and following the distribution of internalized TfR and CD59 by "pulse-chase," we provide evidence suggesting that some of the endosomes at the ERC are linked by "membrane bridges" as long as 500 nm. On the other hand, other endosomes appear to be individual structures and have no detectable Rab11a or cellubrevin

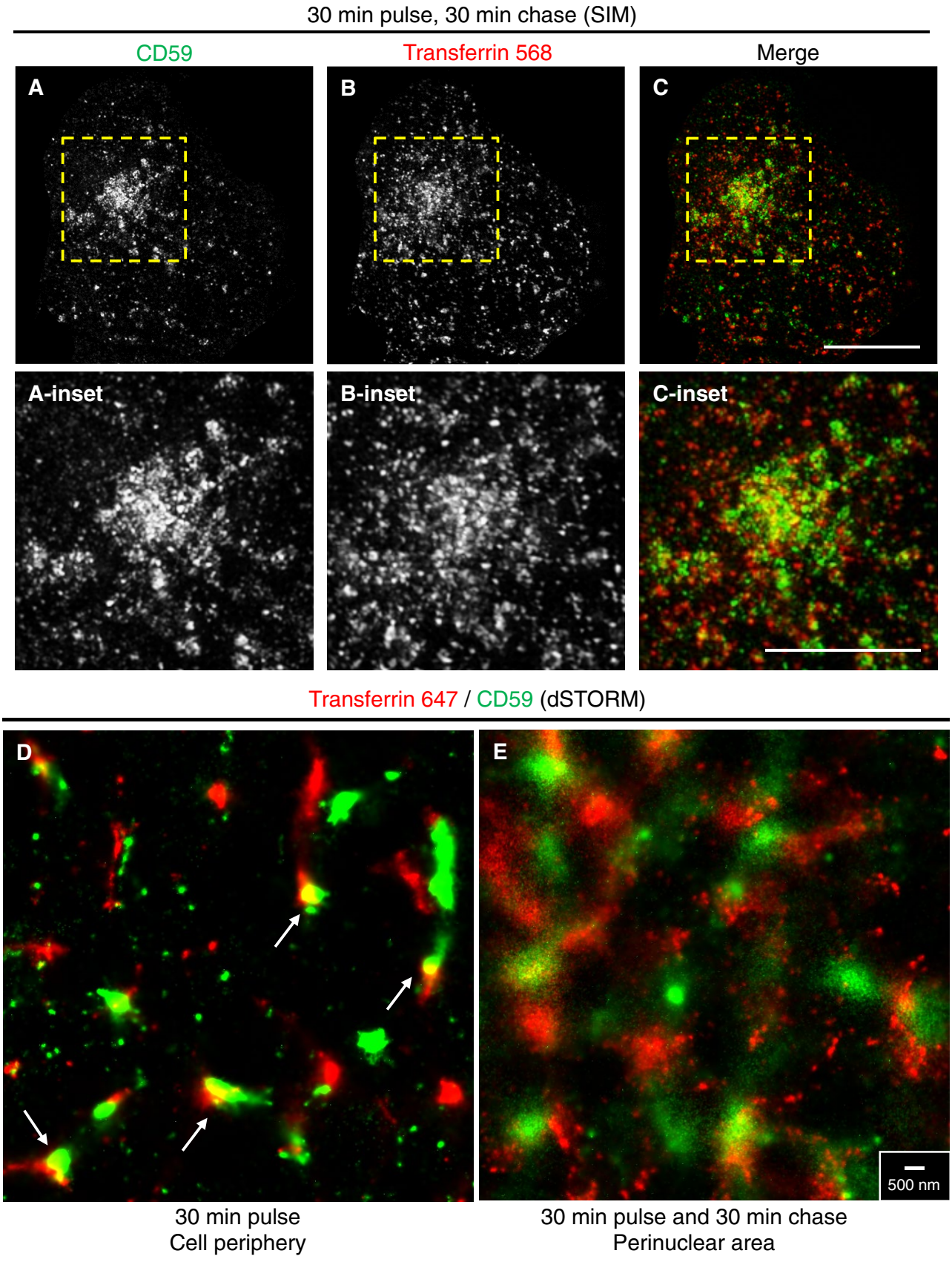

FIGURE 4: Segregation of CME and CIE cargoes in the ERC. (A–C) HeLa cells were serum starved for 1 h and then incubated with anti-CD59 antibody (A) and Alexa 568–conjugated transferrin for 30 min at 37°C (B) and then acid stripped. The cells were then incubated in fresh medium for 30 min before fixation. CD59 was visualized with Alexa 488–conjugated mouse secondary antibody (A). The cells were subjected to SIM analysis. Dashed boxes denote the

"linking" them. Although tomography will be needed to ascertain the individual nature of these vesicles, the ERC appears to comprise of a network of both partially connected and individual vesicles and tubules. While the issue of ERC continuity cannot be entirely resolved from our study, our data are consistent with the notion that the ERC maintains segregation of CME and CIE cargo. Moreover, we demonstrate that whereas CME cargoes are transported to the PM via myosin Vb/Rab11a-FIP2/Rab11a complexes, CIE cargoes are recycled independently of Rab11a and myosin Vb. Overall these findings hint at the intriguing possibility that CIE may be coupled directly to microtubules, whereas CME may rely first on a connection with myosin Vb and microfilaments before being linked to microtubule-dependent transport to the cell surface.

The selectivity of TREs

The routes for cargo entry into the cell have been studied intensively and can be categorized into two very general mechanisms, CME and CIE, depending on whether the clathrin-coated pits are assembled during endocytosis (see model in Figure 11). In comparison to the "canonical" internalization via CME, CIE controls the internalization of distinct cargoes and is mediated by a different set of regulatory proteins and lipids (Mayor *et al.*, 2014). However, much less is known about the fates and itineraries of these proteins and lipids after their entry via different internalization mechanisms. Some regulatory proteins were identified that regulate the recycling of CIE cargoes, such as Rab22a (Weigert *et al.*, 2004), Rab8 (Hattula *et al.*, 2006), and Arf6 (Radhakrishna and Donaldson, 1997; Powelka *et al.*, 2004). Although potentially selective for CIE cargo, these regulators may also exert a regulatory role in the recycling of CME cargoes such as TfR (Hattula *et al.*, 2006; Magadan *et al.*, 2006). We determined that the TRE biogenesis proteins MICAL-L1 and its interaction partner syndapin2 serve as markers for TREs that selectively transport CIE cargoes from SEs into the ERC in addition to their role in regulating ERC-to-PM trafficking. Moreover, MICAL-L1 and the CIE cargoes remain in segregated endosomal structures throughout their retention in the ERC and as they recycle back to the PM. Our data are consistent with the notion that additional sorting at the ERC is unlikely to occur once cargo has exited the SEs. Accordingly, once sorting has been established, cargoes remain in distinct endosomes or regions of the ERC and are returned to the PM independently of one another. These findings shed new light on the mechanism of cargo sorting into different REs.

How are select CME cargoes sorted to Rab11a-decorated membranes, whereas CIE cargoes localize to MICAL-L1–containing TREs at the SEs? Potential mechanisms distinguishing CME and CIE cargoes at the SEs include the following: 1) Cargoes entering through CME often contain signals in their cytoplasmic domains that are recognized by specific regulatory proteins such as ACAP1 (Dai *et al.*, 2004). It is possible that there are regulators for the recognition of CIE cargoes that have yet to be identified. 2) The lipid microenvironment that escorts CME and CIE cargoes from the PM to SEs differs. Vesicles derived from CME typically contain phosphatidylinositol-(4,5)-bisphosphate from the PM (Antonescu *et al.*, 2011). On the other hand, generation of tubular invaginations bearing CIE cargoes is often from cholesterol-enriched domains (Donaldson *et al.*, 2009). In addition, MICAL-L1 is recruited onto the membrane of TREs by PA (Giridharan *et al.*, 2013). The differential lipid microenvironments of recycling endosomes likely also account for the longer and wider tubular structures observed in TREs.

The significance of TREs in endocytic trafficking

Tubular endocytic carriers play an important role in mediating transport within the endocytic pathways (Chi *et al.*, 2015). We identified MICAL-L1 as a TRE marker that stably resides on the endosomal membrane and facilitates its tubulation and biogenesis (Sharma *et al.*, 2009). MICAL-L1–decorated TREs bear different lipid components than the tubular invaginations at the PM, and MICAL-L1 does not localize to PM tubules labeled by WGA (Supplemental Figure S5; Flesch *et al.*, 1998). Indeed, TRE are crucial for the recycling of internalized receptors and lipids. Because depletion of either MICAL-L1 or EHD1 resulted in the failure of TfR and β1-integrin to exit the ERC, TREs have been primarily considered as carriers of cargoes returning to the PM from the ERC (Jovic *et al.*, 2007; Donaldson *et al.*, 2009; Sharma *et al.*, 2009). Despite this evidence, the directionality and transport itinerary of TRE have not been firmly established, and whether TRE might also support SE-to-ERC trafficking has been an open question until now.

Our study demonstrates that MICAL-L1–decorated TRE can be generated from Rabenosyn-5–containing SEs, suggesting that TREs are responsible for the movement of cargo from peripheral SEs to the perinuclear ERC (see model in Figure 11). Furthermore, MICAL-L1 recruits EHD1 to the TRE membrane, which mediates the fission of tubules and supports vesicular transport (Naslavsky and Caplan, 2011). Our findings indicate that cargo-containing TREs can originate from SEs and that EHD1 likely cleaves TREs to generate vesicular endosomes that ultimately bring in cargoes to the ERC. This notion is reinforced by the imaging of TREs either by SIM or dSTORM (Figure 7) and by live imaging (Figure 10). In these images, MICAL-1 localizes to a contiguous tubular membrane in the cell periphery, whereas it resides on more vesicular structures in the perinuclear area.

As noted, the effect of either MICAL-L1 or EHD1 depletion leads to cargo accumulation in the ERC. These phenotypic observations fit a model in which TREs facilitate the *exit* of cargo from the ERC rather than the transport of cargo *into* the ERC. This raises the question of why cargo appears to be delayed at the ERC rather than the SE. One possibility is that TRE might bidirectionally transport cargoes both *to* and *out of* the ERC. In this scenario, we hypothesize that cargo at the SEs has various compensatory or alternate pathways to reach the ERC (in the absence of EHD1 or MICAL-L1) but fewer alternate pathways to exit the ERC. Thus the absence of MICAL-L1/EHD1 may induce nonphysiological transport of cargo to the ERC via alternate pathways but then cause the cargo to remain trapped within the ERC. Indeed, impaired function of Rab11, which appears to be involved in sorting at the SEs (Sonnichsen *et al.*, 2000) as well as ERC-to-PM trafficking, also causes accumulation of cargo at the ERC (Ren *et al.*, 1998). It has been proposed that EHD proteins mediate membrane scission upon ATP hydrolysis (Daumke *et al.*, 2007). In this scenario, EHD1 depletion would impair TRE

perinuclear area where CD59 and TfR were highly concentrated. Insets, magnified images of the boxed areas. Scale bars, 10 μm. (D, E) HeLa cells plated on glass-bottom MatTek dishes were serum starved for 1 h, followed by incubation of anti-CD59 antibody, as well as of Alexa 647–conjugated transferrin, for 30 min at 37°C. Then the cells were acid stripped and either fixed (D; periphery) or chased in fresh medium for 30 min before fixation (E; perinuclear area). The plates were then incubated with Atto 488–conjugated anti-mouse antibody. dSTORM was performed by acquiring $>1 \times 10^6$ localizations during >20,000 frames obtained every 50 ms. The single-molecule localizations were reconstructed into a normalized Gaussian image at 10-nm pixel size using the ThunderSTORM plug-in in ImageJ. Scale bar, 500 nm.

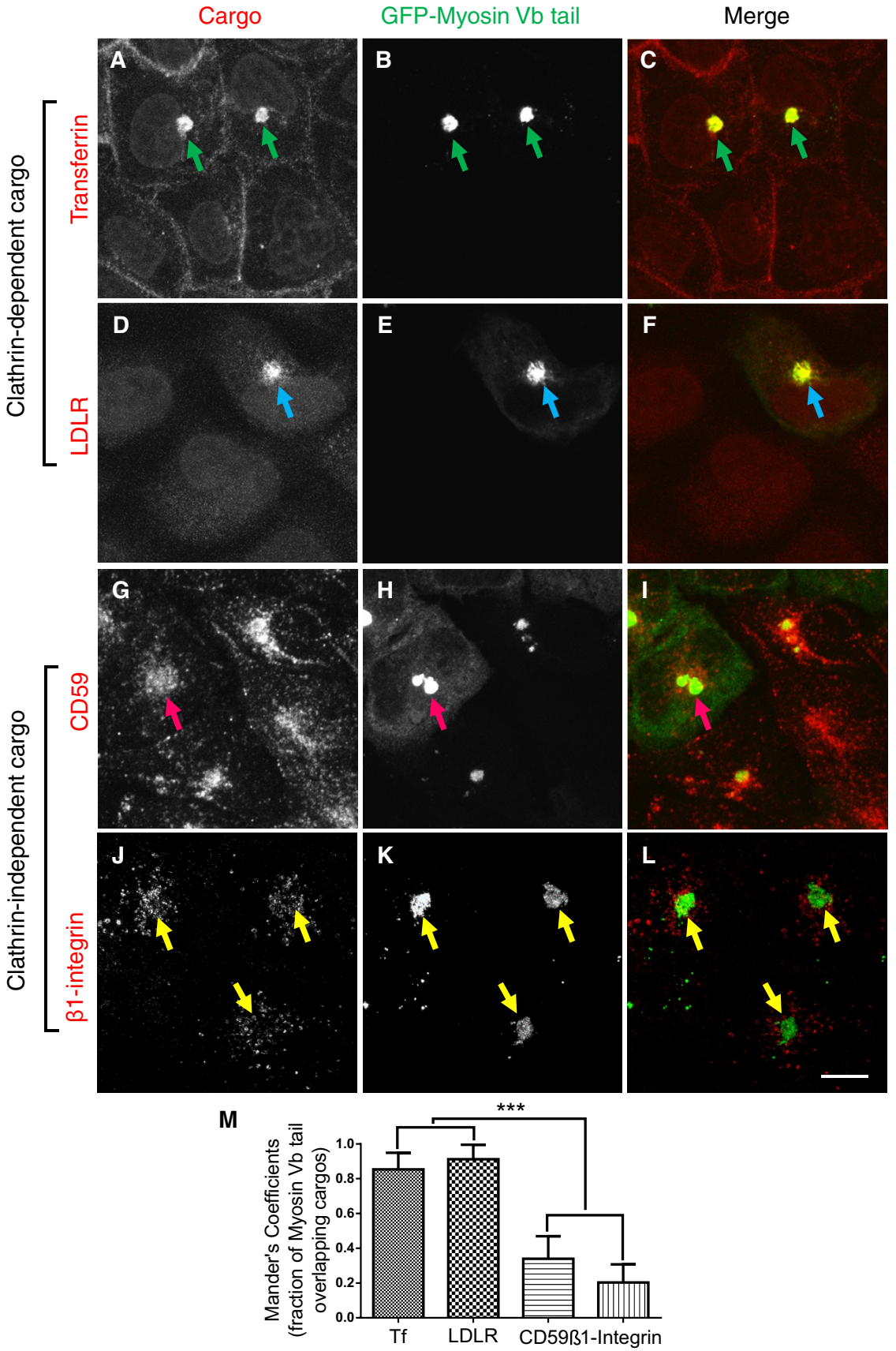

FIGURE 5: Myosin Vb tail overexpression selectively traps CME cargoes in the perinuclear area. (A–C) HeLa cells transfected with GFP–myosin Vb tail were incubated with transferrin for 30 min at 37°C, washed, and then incubated in fresh medium for 2 h. Green arrows point to the perinuclear area where TfR (A) colocalized with the GFP–myosin Vb tail (B). (D–F) HeLa cells transfected with GFP–myosin Vb tail were incubated with anti-LDLR antibody for 30 min

vesiculation, and we speculate that this process might also be essential for exit of recycling cargo from the ERC once cargo has arrived from the SEs.

Another potential reason for cargo accumulation at the ERC (as opposed to the peripheral SEs) upon EHD1 or MICAL-L1 depletion is that it might result from the coalescence of entire SE populations into the ERC region. A study from our lab suggested that MICAL-L1 is linked to dynein-mediated trafficking via the collapsin response mediator protein 2 (CRMP2) and that MICAL-L1 or CRMP2 depletion led to more rapid cargo transport to the ERC (Rahajeng *et al.*, 2010). We cannot rule out the possibility that intact peripheral SEs migrate and cluster to the ERC region; if this is the case, then one explanation for delayed cargo recycling at the ERC upon EHD1 or MICAL-L1 depletion could be failure of the cargo to exit intact SEs that have already migrated and coalesced into the ERC region. It is of interest that recycling endosomes are tightly connected with the appendages of the mother centriole, since they are both found in the perinuclear region (Hehnly *et al.*, 2012). Accordingly, we hypothesized that MICAL-L1 and EHD1 might serve as a link between RE and centrosomes (Reinecke *et al.*, 2015). MICAL-L1/EHD1 may have a nonselective effect on RE attachment to the microtubules for transportation to the PM and thus contribute to the regulation of endocytic recycling from the ERC.

Our studies alter the current understanding of the role that TREs play in endocytic recycling. Because we view receptor sorting as less likely to occur in the ERC, we speculate that the transport of endosomes to this central area of the cell may serve to focus REs at a "staging ground" where REs (from both CME and CIE) are linked to microtubule tracks and/or the actin cytoskeleton by select motor proteins (see model in Figure 11). Accordingly, the involvement of myosin Vb in CME trafficking hints at a possible requirement for both microfilament- and microtubule-dependent transport mechanisms, whereas we predict that CIE might rely more exclusively on microtubules. Although future studies are needed to address this idea, we speculate that the ERC region provides a concentrated platform on which vesicles/tubules, motor proteins, and the cytoskeleton may be coupled to facilitate efficient transport to the PM.

MATERIALS AND METHODS

Cell lines

HeLa cells from the American Type Culture Collection (Manassas, VA) were grown in DMEM containing 10% fetal bovine serum, 2 mM glutamine, 100 U/ml penicillin, and 100 U/ml streptomycin.

DNA constructs, transfection, and small interfering RNA treatment

Human hemagglutinin (HA)-MICAL-L1 and HA-syndapin2 were previously described (Sharma *et al.*, 2009; Giridharan *et al.*, 2013). The green fluorescent protein (GFP)–myosin Vb tail construct was a gift from James R. Goldenring (Vanderbilt University Medical Center, Nashville, TN; Lapierre *et al.*, 2001). GFP-cellubrevin was kindly provided by J. Donaldson (National Heart, Lung, and Blood Institute, National Institutes of Health, Bethesda, MD). Dominant-negative GFP-Rab11 (S25N) was kindly provided by Robert Lodge (University of Montreal, Montreal, Canada). HeLa cells were transfected for 18 h at 37°C with X-tremeGENE 9 (Roche Applied Science, Indianapolis, IN) according to the manufacturer's protocol. Small interfering RNA (siRNA) oligonucleotides targeting human Rab11A were synthesized by Dharmacon (Lafayette, CO): sense (5′-GAGUAAUCUCCUGUCUCGA(dT)(dT)-3′). Rab11a-siRNA treatment was carried out with Lipofectamine RNAiMAX (Invitrogen, Carlsbad, CA) for 48 h according to the manufacturer's protocol, using 0.3 μM oligonucleotide (Dharmacon).

Antibody and reagents

Mouse monoclonal MEM-43 ascites antibody against CD59 was kindly provided by V. Horejsi (Academy of Sciences of the Czech Republic, Prague, Czech Republic) and used previously (Cai *et al.*, 2011, 2012, 2014). Other commercial antibodies used were mouse anti-human β1-integrin (CD29; AbD Serotec, Raleigh, NC), rabbit anti-LDLR (Progene, Lenexa, KS), mouse anti-human TfR (Zymed, Lafayette, CO), mouse anti–MICAL-L1 (Novus Biologicals, Littleton, CO), mouse anti-actin (Novus Biologicals), rabbit anti–Rabenosyn-5 (Novus Biologicals), rabbit anti-Rab11a (US Biologicals, Salem, MA), rabbit anti-HA (Signalway, College Park, MD), goat anti-mouse horseradish peroxidase (HRP; Jackson ImmunoResearch Laboratories, West Grove, PA), donkey anti-rabbit HRP (GE Healthcare, Pittsburgh, PA), and Alexa 568–conjugated goat anti-mouse, Alexa 488–conjugated goat anti-rabbit. Secondary antibodies used in dSTORM imaging were Alexa 647 goat anti-mouse $F(ab)_2$ (Invitrogen), Atto 488–conjugated anti-rabbit (Sigma-Aldrich, St. Louis, MO), Atto 488–conjugated anti-mouse (Sigma-Aldrich), and Alexa 647 goat anti-rabbit (Life Technologies, Carlsbad, CA). Anti-CD59 antibody was conjugated to Alexa 555 with the APEX Alexa Fluor 555 Antibody Labeling Kit (Life Technologies) according to the manufacturer's instructions.

Reagents used include Alexa 568–conjugated transferrin, Alexa 633–conjugated transferrin, Alexa 647–conjugated transferrin, and WGA from Life Technologies, CAY inhibitor cocktail (CAY10593, CAY10594) from Cayman Chemical Company (Ann Arbor, MI), and 20% glucose solution, glucose oxidase from *Aspergillus niger*, catalase from bovine liver, cysteamine hydrochloride (MEA), and 100-nm-diameter gold nanoparticles, all purchased from Sigma-Aldrich.

Immunoblotting

HeLa cells were harvested and lysed on ice for 30 min in lysis buffer containing 50 mM Tris, pH 7.4, 150 mM NaCl, 1% Nonidet P-40, 0.5% sodium deoxycholate, and protease inhibitor mixture (Roche Molecular Biochemicals). Total protein levels in the lysate were then determined by Bio-Rad protein assay (Bio-Rad Laboratories,

at 37°C and then acid stripped and incubated in fresh medium for 2 h. Blue arrows point to the perinuclear area where LDLR (D) colocalized with the GFP–myosin Vb tail (E). (G–I) HeLa cells transfected with GFP–myosin Vb tail were incubated with CD59 for 30 min at 37°C and then acid stripped and incubated in fresh medium for 2 h. Magenta arrows point to the perinuclear area where GFP–myosin Vb tail (H) is highly compact, whereas CD59 (G) displayed limited localization to this region. (J–L) HeLa cells transfected with GFP–myosin Vb tail were incubated with β1-integrin for 30 min at 37°C, acid stripped, and incubated in fresh medium for 2 h. Yellow arrows denote the perinuclear area where β1-integrin (J) showed limited colocalization with the GFP–myosin Vb tail (K). Scale bar, 10 μm. (M) The degree of colocalization between GFP–myosin Vb tail and different cargoes was measured using ImageJ with Manders overlap coefficients. One hundred twenty cells from three independent experiments were measured and subjected to statistical analysis. Error bars, SD. ***$p < 0.0005$.

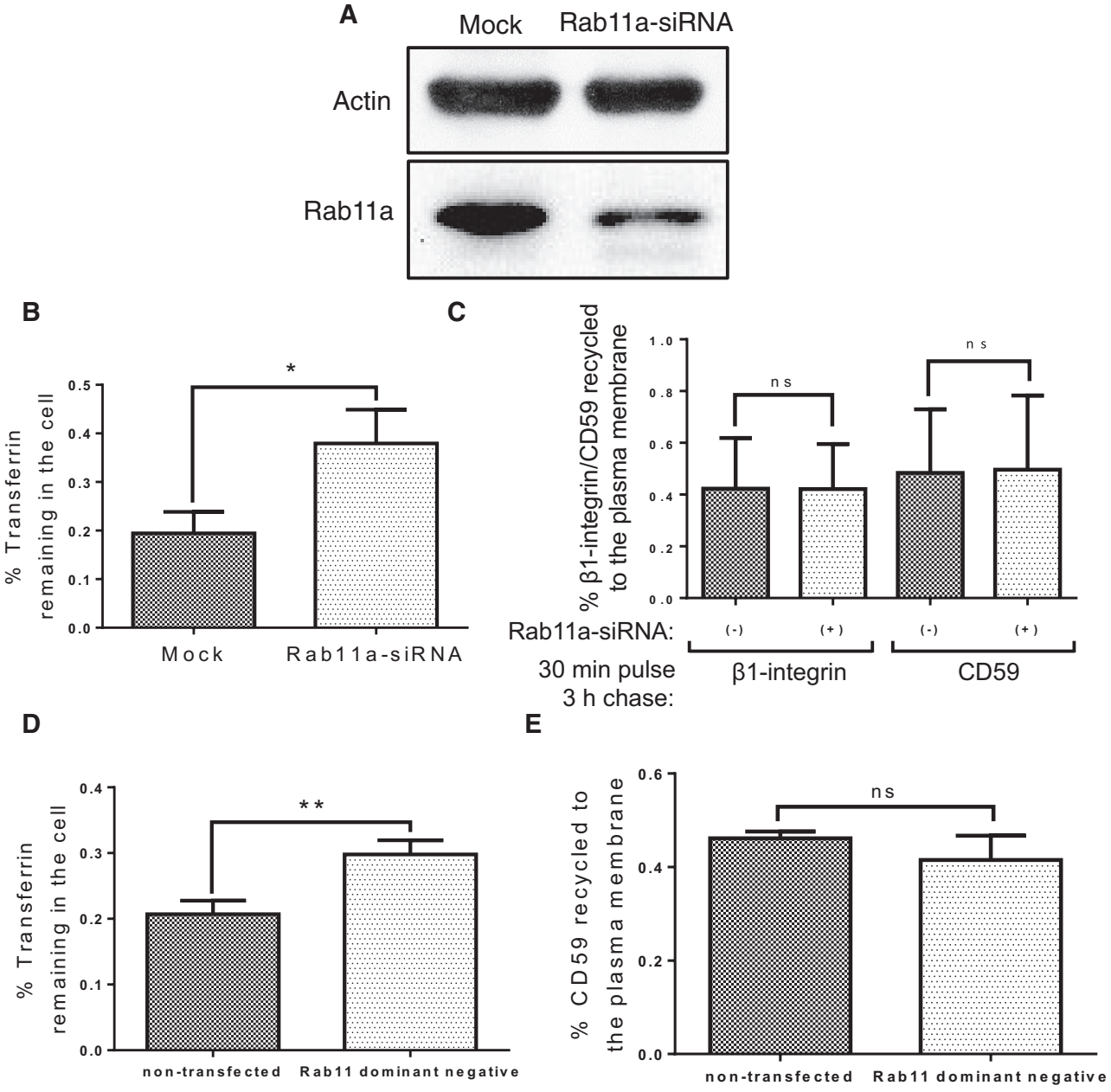

FIGURE 6: Rab11a regulates the recycling of CME but not CIE cargo. (A) HeLa cells were treated with siRNA against Rab11a for 48 h before cell lysis. Rab11a expression was measured by immunoblotting. Actin was used as a loading control. (B) Mock- and Rab11a siRNA–treated cells were serum starved for 1 h, pulsed with Alexa 633–conjugated transferrin for 1 h at 37°C, and then chased in fresh medium for 30 min. The remaining transferrin in the cell was measured by flow cytometry. Statistical analysis was performed with data from three independent flow cytometry assays. SD is shown. *$p < 0.05$. (C) Mock- and Rab11a siRNA–treated cells were pulsed with anti–β1-integrin or anti-CD59 antibody for 30 min at 37°C, acid stripped, and chased for 3 h before fixation. The cells were then stained with Alexa 568 anti-mouse antibody in the absence of saponin. The total levels of β1-integrin and CD59 were also measured with fixed cells incubated with anti–β1-integrin or anti-CD59 antibody in the presence of saponin. The return of β1-integrin/CD59 to the cell surface after a 3-h chase was calculated as a portion of the total protein level. One hundred eighty cells from three independent experiments were analyzed with ImageJ. Bars indicate SD. (D) HeLa cells transfected with dominant-negative GFP-Rab11 (S25N) were serum starved for 1 h, pulsed with Alexa 568–conjugated transferrin for 1 h at 37°C, and then chased in fresh medium for 30 min. The samples were imaged by confocal microscopy, and the remaining transferrin in nontransfected and dominant-negative GFP-Rab11–transfected cells was determined by ImageJ intensity measurements. SD is shown. **$p < 0.01$. (E) HeLa cells transfected with dominant-negative GFP-Rab11 (S25N) were pulsed with anti-CD59 antibody for 30 min at 37°C, acid stripped, and chased for 3 h before fixation. The cells were then stained with Alexa 568 anti-mouse antibody in the absence of saponin. The total levels of CD59 were also measured with fixed cells incubated with anti-CD59 antibody in the presence of saponin. The return of CD59 to the cell surface after a 3-h chase was calculated as a portion of the total protein level. One hundred twenty cells from three independent experiments were analyzed with ImageJ. SD is shown.

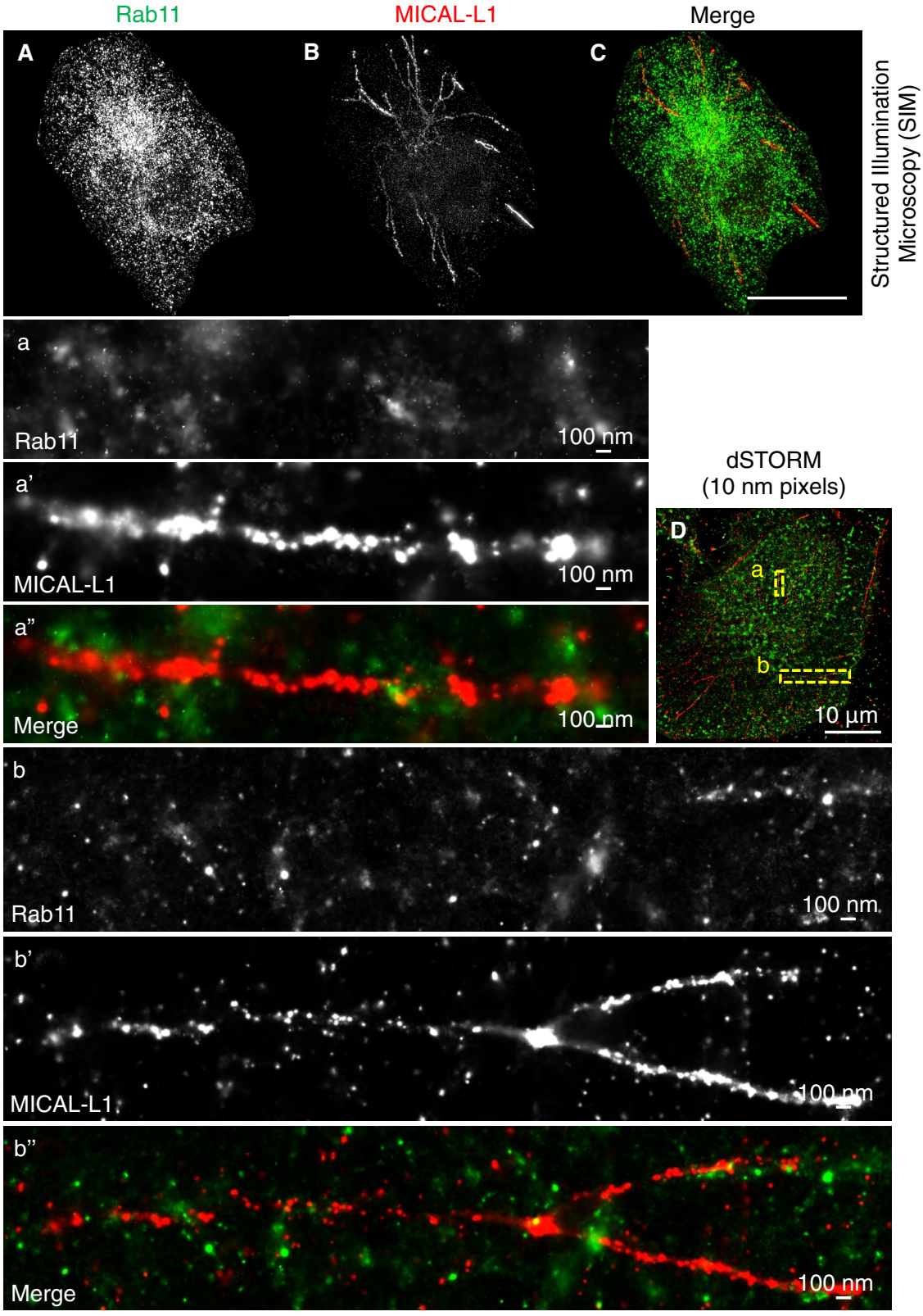

FIGURE 7: SIM and dSTORM visualization of Rab11a and MICAL-L1–labeled TREs. (A–C) HeLa cells were stained with anti-Rab11a and anti-MICAL-L1 together with the corresponding secondary antibody and imaged by SIM. Scale bar, 10 µm. (D) Reconstructed dSTORM image showing Rab11a and MICAL-L1 in the perinuclear area (a–a″) and in the periphery (b–b″). HeLa cells plated on glass-bottom MatTek dishes were fixed and stained with anti-Rab11a and anti–MICAL-L1 antibodies, followed by Atto 488–conjugated anti-rabbit and Alexa 647–conjugated anti-mouse antibody. dSTORM was performed by acquiring >1 × 10^6 localizations during >20,000 frames obtained every 50 ms. The single-molecule localizations were reconstructed into a normalized Gaussian image with a pixel size of 10 nm using the ThunderSTORM plug-in in ImageJ. The entire cell from where these images are cropped is shown in D (dashed rectangles a and b).

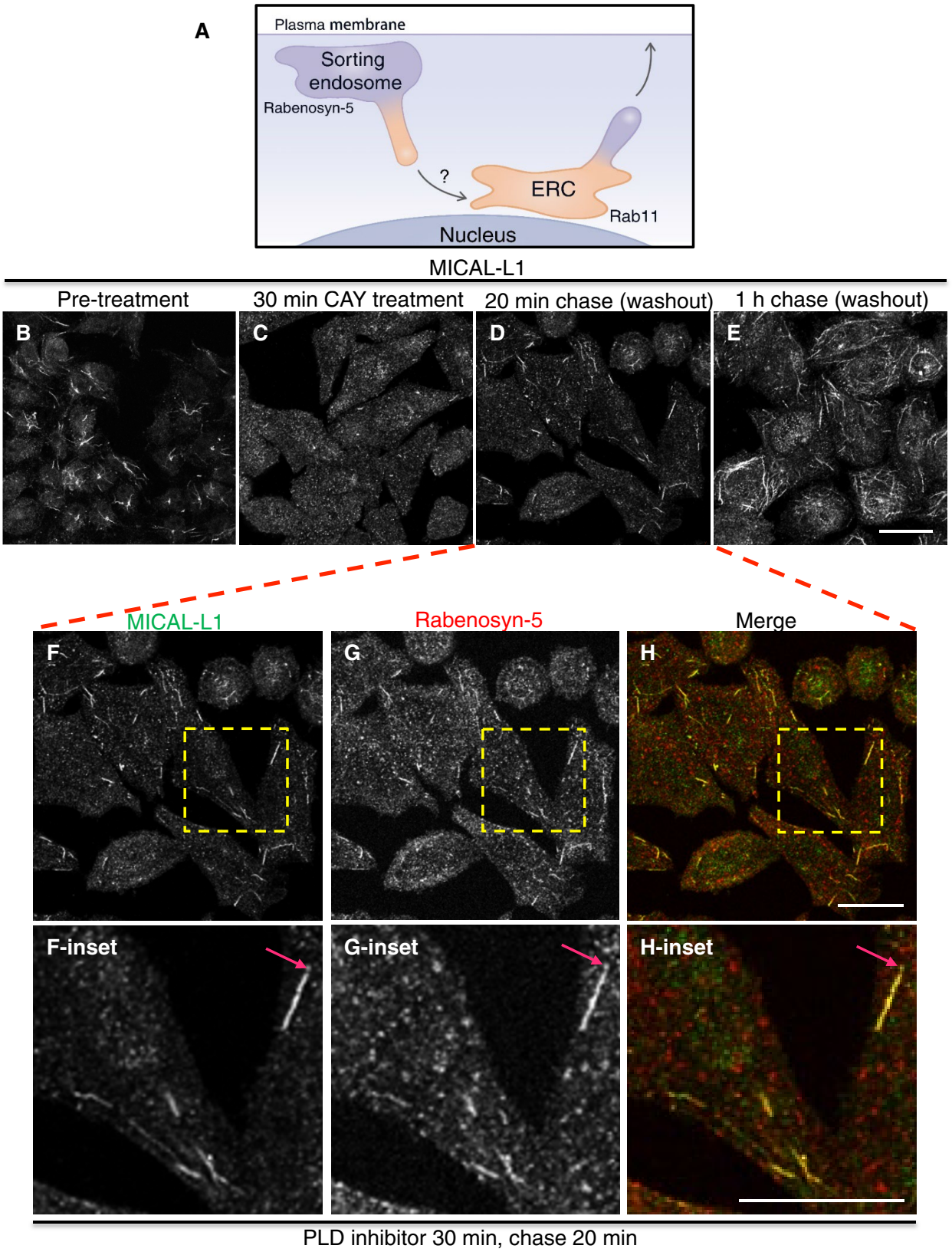

FIGURE 8: MICAL-L1–decorated TRE are derived from SEs. (A) Schematic diagram depicting the ERC and potentially SEs as likely sources of TRE membrane. (B–E) TRE analysis by confocal microscopy was done on (B) untreated cells, (C) cells incubated with phospholipase D inhibitors for 30 min, or (D) after inhibitor washout and chase in fresh DMEM for 20 min (D) or 1 h (E). Scale bar, 10 μm. (F–H) TREs colocalized with the endosomal marker Rabenosyn-5 upon regeneration. HeLa cells treated with PLD inhibitors for 30 min and then chased in fresh DMEM for 20 min (as in D) were costained with MICAL-L1 (F) and Rabenosyn-5 (G) antibodies. Arrows depict the nucleation of a MICAL-L1–containing TREs from a Rabenosyn-5–endosome. Scale bars, 10 μm.

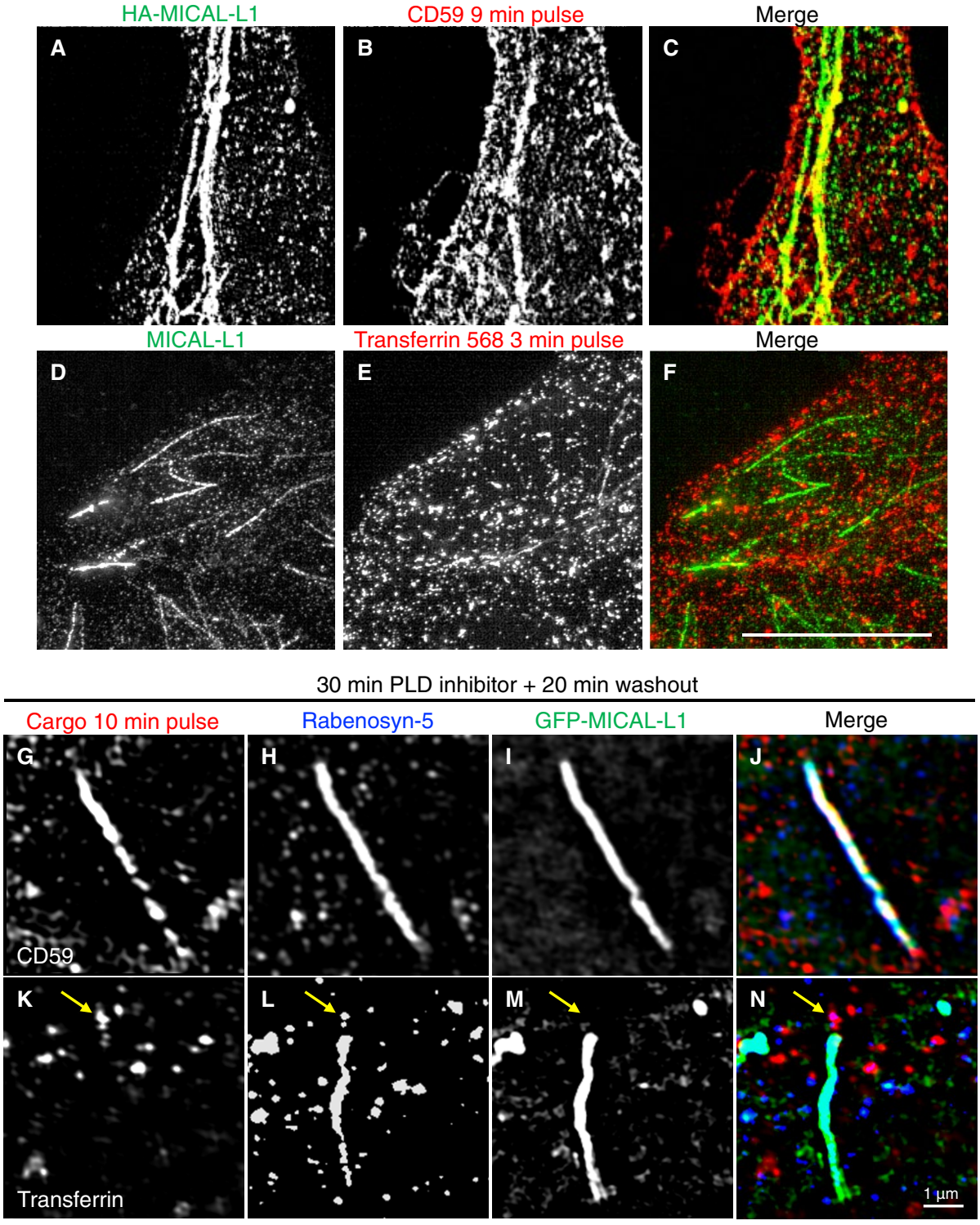

FIGURE 9: TREs selectively transport cargoes from SE. (A–F) HeLa cells on coverslips were transiently transfected with HA-MICAL-L1 for 18 h and incubated with anti-CD59 antibody for 9 min at 37°C (A–C) or pulsed for 3 min with Alexa 568–conjugated transferrin (D–F). Surface-bound CD59 antibody was removed by acid strip before fixation. Internal CD59 was visualized with Alexa 568–conjugated anti-mouse antibody (B) in the presence of saponin. MICAL-L1 was visualized with rabbit anti-HA antibody and Alexa 488–conjugated anti-rabbit antibody (A). Scale bar, 10 µm. (G–N) HeLa cells transfected with GFP–MICAL-L1 were treated for 30 min with PLD inhibitors and then either incubated with mouse anti-CD59 antibody for 10 min at 37°C, followed by staining with Alexa 568–conjugated anti-mouse antibody (G–J), or incubated with Alexa 568–conjugated transferrin for 10 min at 37°C. Rabenosyn-5 endosomes were detected by rabbit anti–Rabenosyn-5, followed by Alexa 647–conjugated anti-rabbit secondary antibody. All images are maximal projections of ~20 SIM slices separated by 110 nm in the *Z*-axis. Arrows in K–N depict TfR in Rabenosyn-5–containing endosomes that are absent from TREs. Scale bar, 1 µm. The degree of colocalization between different cargoes and Rabenosyn-5 or MICAL-L1 is quantified and summarized in Supplemental Figure S6, D and E.

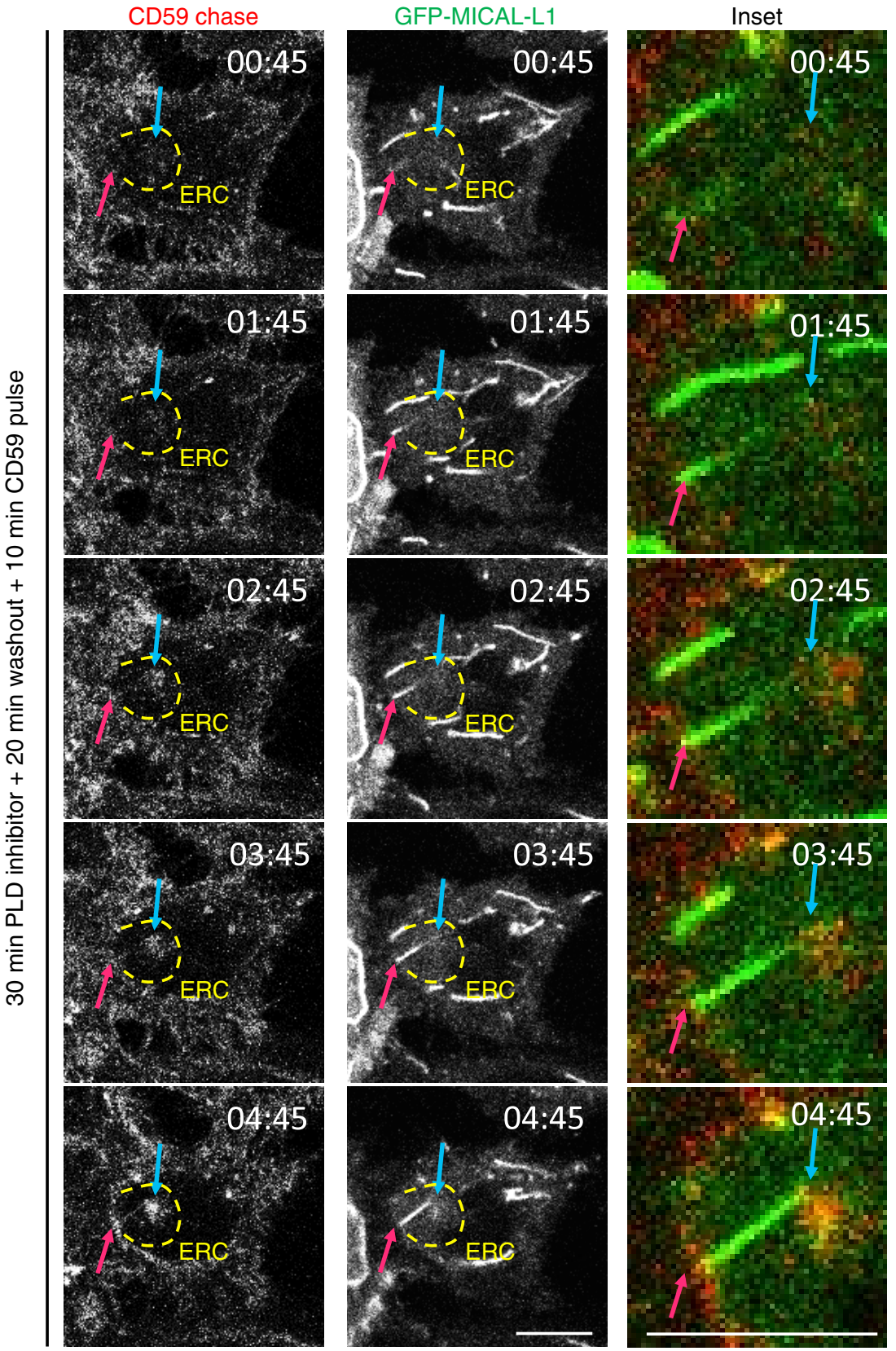

FIGURE 10: TREs transport CD59 into the recycling compartment. HeLa cells on 35-mm glass-bottom plates were transiently transfected with GFP–MICAL-L1 for 18 h and incubated with PLD inhibitors for 30 min at 37°C. The cells were then washed three times and incubated in fresh complete medium for 10 min at 37°C, followed by a 10 min-pulse of Alexa 555–conjugated anti-CD59 antibody. The cells were then washed and imaged in prewarmed Ringer's solution. Red arrows indicate the initiation site of a newly generated MICAL-L1-TRE. Blue arrows point to the growing ERC. Dashed boxes denote the perinuclear area and are shown with higher magnification in the insets. Scale bars, 10 μm.

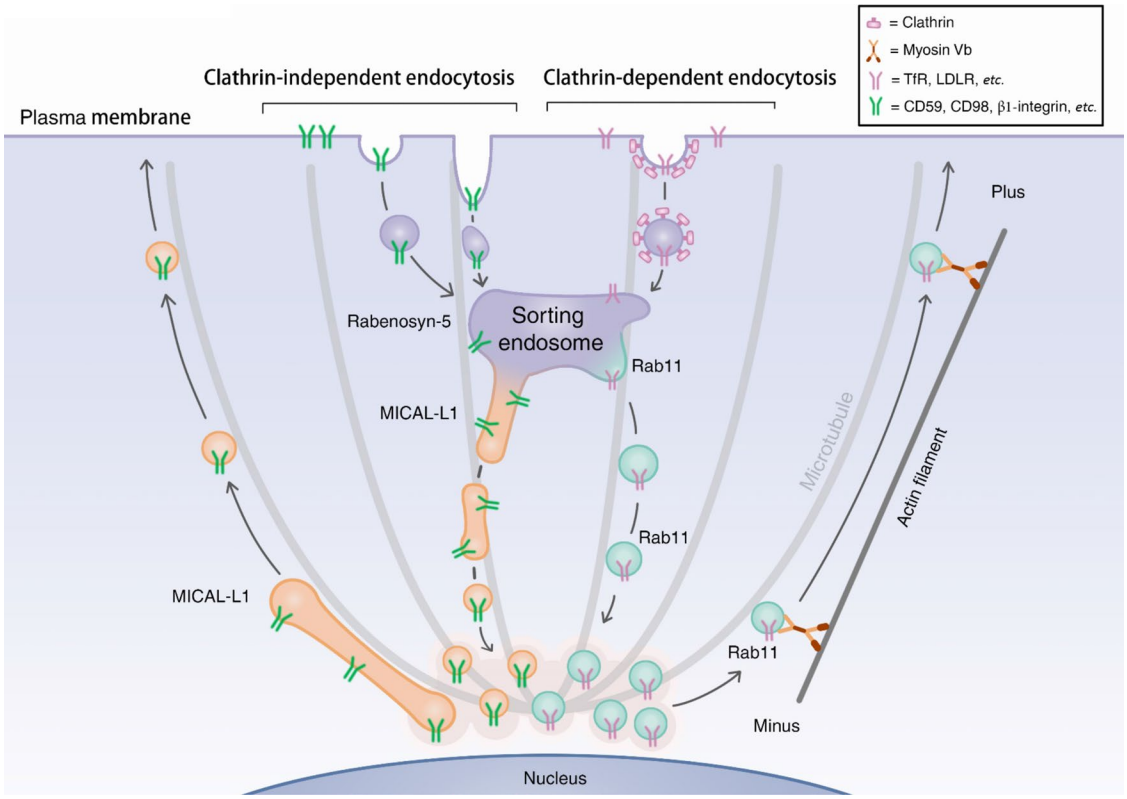

FIGURE 11: Proposed model depicting the recycling of CME and CIE. Cargoes internalized through CME and CIE merge in Rabenosyn-5–containing sorting endosomes (SEs). Rab11a vesicles (or small labile tubules) are formed to escort CME cargoes such as TfR and LDLR to the perinuclear area. MICAL-L1–decorated TREs are also generated from Rabenosyn-5–containing SEs, carrying CIE cargoes such as CD59, CD98, and β1-integrin to the perinuclear area. The sorted cargoes remain segregated in the dense perinuclear ERC. Cargoes are then linked to motor proteins along microtubules in either vesicular or tubular recycling endosomes and transported back to the PM.

Hercules, CA) and normalized for equal protein loading on gels. Protein samples were separated on 10% SDS–PAGE and detected by immunoblotting with appropriate antibodies.

Immunofluorescence staining

Cells grown on coverslips were fixed with 4% (vol/vol) paraformaldehyde in phosphate-buffered saline (PBS) for 10 min as previously described (Xie *et al.*, 2014). Cells were then incubated with primary antibody in staining buffer containing 0.2% saponin (wt/vol) and 0.5% bovine serum albumin (wt/vol) in PBS for 1 h at room temperature. The appropriate fluorochrome-conjugated secondary antibody was applied in the same staining buffer for 1 h at room temperature. Coverslips were mounted on glass slides in Fluoromount G (SouthernBiotech, Birmingham, AL). Confocal microscopy imaging was done with a Zeiss LSM 5 Pascal confocal microscope (Carl Zeiss, Oberkochen, Germany) using a 63× objective with a numerical aperture (NA) of 1.4 and appropriate filters, and SIM was done with a Zeiss Elyra PS.1 Microscope (Carl Zeiss) by using a 63× objective with NA of 1.4. To measure colocalization, at least 60 cells from three independent confocal microscopy experiments or 12 cells from three independent SIM experiments were assessed using ImageJ (National Institutes of Health, Bethesda, MD) with Manders colocalization using the JaCoP plug-in.

For dSTORM sample preparation, cells plated on glass-bottom MatTek dishes were fixed and stained with primary antibody in staining buffer, washed, and then incubated with secondary antibody. The stained cells were fixed again for 10 min in 4% (vol/vol) paraformaldehyde and incubated in presonicated 100-nm-diameter gold nanoparticles for 20 min at room temperature before dSTORM acquisition.

Live-cell imaging

HeLa cells on 35-mm glass-bottom tissue culture dishes (World Precision Instruments, Sarasota, FL) were transiently transfected with GFP-MICAL-L1 for 18 h and incubated with PLD inhibitors for 30 min at 37°C. The cells were then washed three times and incubated in fresh complete medium for 10 min at 37°C, followed by a 10-min pulse of anti-CD59 antibody conjugated with Alexa 555. Then the cells were washed and imaged in prewarmed Ringer's solution (152 mM NaCl, 25 mM 4-(2-hydroxyethyl)-1-piperazineethanesulfonic acid, pH 7.4, 5.6 mM glucose, 4.8 mM KCl, 1.3 mM $CaCl_2$, 1.2 mM KH_2PO_4, 1.2 mM $MgSO_4$) covered by a thin layer of mineral oil. Confocal microscopy imaging was done with a Zeiss LSM 5 Pascal confocal microscope (Carl Zeiss) using a 63× objective with NA of 1.4 and appropriate filters. Images in each channel were obtained at 512 × 512 pixels with the pinhole set at z-slices of 1.6 µm. The imaging was performed every 15 s, and images taken at 45 s; 1 min, 45 s; 2 min, 45 s; 3 min, 45 s; and 4 min, 45 s are presented.

Structured illumination microscopy imaging and data processing

SIM images were collected with a Zeiss ELYRA PS.1 illumination system (Carl Zeiss) using a 63× oil objective lens with NA of 1.4. Three lasers were used in the image acquisition: 642, 568, and 488 nm.

Pixel size (nm)	200
Photoelectron per A/D count	7.0
Base level (A/D count)	100.0
EM gain	250.0
Filter	Wavelet filter (B-spline)
B-spline order	3
B-spline scale	2.0
Approximate localization of molecules	
Method	Local maximum
Peak intensity threshold	Std(Wave.F1)
Connectivity	Eight-neighborhood
Subpixel localization of molecules	
Method	PSF: integrated Gaussian
Fitting radius (pixels)	3
Fitting method	Least squares
Initial sigma (pixels)	1.6

TABLE 1: Parameters used in the ThunderSTORM analysis.

Three orientation angles of the excitation grid were acquired for each *Z*-plane, with *Z* spacing of 110 nm between planes.

SIM processing was performed with the SIM module of the Zen BLACK software (Carl Zeiss). The processed SIM images were then exported in TIF format. Selected cell regions were cropped in ImageJ, rendered into a 3D reconstruction with a 180-frame rotation series along the *Y*-axis of the processed SIM images, and exported as AVI videos.

Pixel size (nm)	320
Photoelectron per A/D count	7.0
Base level (A/D count)	100.0
EM gain	250.0
Filter	Wavelet filter (B-spline)
B-spline order	3
B-spline scale	2.0
Approximate localization of Molecules	
Method	Local maximum
Peak intensity threshold	2*Std(Wave.F1)
Connectivity	Eight-neighborhood
Subpixel localization of molecules	
Method	Elliptic Gaussian with angle
Fitting radius (pixels)	3
Fitting method	Least squares
Initial sigma (pixels)	1.6
3D defocus model	ThunderSTORM
Z stage step (nm)	10.0
Z-range limit (nm)	4000.0

TABLE 2: Parameters used in the 3D dSTORM calibration.

dSTORM imaging and data processing

dSTORM was performed on a Zeiss Elyra PS.1 microscope with a 100× oil-immersion objective with 1.46 NA. For the imaging of Alexa 647 and Atto 488, we used 642-, 488-, and 405-nm laser lines. Cell samples were kept in imaging buffer (50 mM Tris, 10 mM NaCl, 10% glucose, pH 8.0) containing 100 mM MEA, 0.56 mg/ml glucose oxidase, and 34 µg/ml catalase and imaged sequentially to detect Alexa 647 and then Atto 488. Images in each channel were obtained at 256 × 256 pixels. The imaging acquisition was performed at 33 Hz. From 10,000 to 25,000 frames were obtained for each channel. The 3D dSTORM was performed as described, except using a 63× oil-immersion objective with 1.4 NA and a 3D-PALM slider. We obtained 40,000 frames for 3D dSTORM.

Acquired data were processed using the ImageJ plug-in ThunderSTORM (Ovesny *et al.*, 2014). The parameters used in the processing are listed in Table 1. Lateral drift was corrected using the ThunderSTORM correlation algorithm, and pixels displaying uncertainty (precision) >60 nm were filtered out before reconstruction to normalized Gaussian images with 10-nm pixel size. Regions of interest (ROIs) were selected, and the number of pixels (*n*) within the ROI and the area (*A*, nm^2) of the ROI were calculated. The Nyquist resolution (*r*) of the ROI was calculated as $r = 2\frac{1}{\sqrt{n/A}}$. The precision for each pixel within the ROI was plotted on the frequency distribution graph with 30 bins.

To carry out dual-channel alignment, at least three fiducial gold nanoparticles fluorescing at both corresponding green and red wavelengths were used for calibration. The lateral (*X* and *Y*) distances for the same particles at the two wavelengths were measured by ImageJ, and the reconstructed image was adjusted accordingly.

Before 3D dSTORM processing, a cylindrical lens calibration was performed. Fiducial gold nanoparticles were plated on glass-bottom MatTek dishes and imaged with 3D dSTORM conditions with a *Z* stage step of 10 nm and 4000-nm *Z*-range limit. The image series was analyzed by Thunderstorm 3D calibration using the parameters listed in Table 2. The calibration files were saved for 3D analysis. The 3D dSTORM processing was carried out using ThunderSTORM with parameters listed in Table 3. The processed data were drift corrected and filtered as described for 2D dSTORM and rendered into normalized Gaussian images with 40 *Z*-slices of 25 nm thickness. Single-slice images were presented.

To validate the image processing, the data collected were reconstructed into normalized Gaussian images with 200-nm pixel size using ThunderSTORM as described. The images were then convolved by a Gaussian blur filter with the mean point spread function (PSF).

Colocalization was determined by ImageJ. Histogram images of both channels with 10-nm pixel size were generated respectively and then aligned as described. The pixels from each image were converted to 0 (no pixel intensity) or 1 (pixel intensity from 1 to 255). Colocalization was defined as a pixel with values of 1 in each channel. Total two-channel represents the number of pixels, and total colocalized is the number of those pixels that have values of 1 in each channel. Degree of colocalization was determined by the ratio of total colocalized to total in two channels.

Histograms representing the calculated uncertainty for each channel were plotted on frequency distribution graphs with 30 bins, and the mode of the plotted curve was calculated as the precision for the image.

Pulse-chase recycling assay

HeLa cells grown on coverslips were incubated with anti–CD59/β1-integrin antibody for 30 min at 37°C (pulse). The surface-bound and

Pixel size (nm)	320
Photoelectron per A/D count	7.0
Base level (A/D count)	100.0
EM gain	250.0
Filter	Wavelet filter (B-spline)
B-spline order	3
B-spline scale	2.0
Approximate localization of molecules	
Method	Local maximum
Peak intensity threshold	2*Std(Wave.F1)
Connectivity	Eight-neighborhood
Subpixel localization of molecules	
Method	PSF: elliptical Gaussian (3D astigmatism)
Fitting radius (pixels)	3
Fitting method	Least squares
Initial sigma (pixels)	1.6

TABLE 3: Parameters used in the 3D dSTORM analysis.

noninternalized antibody was removed by a 1-min acid strip (0.5 M NaCl, 0.5% acetic acid, pH 3.0). The cells were then incubated in complete medium for the indicated times at 37°C (chase) and then washed three times in PBS before fixation. An additional coverslip was treated with only 30-min pulse and acid strip to determine the initial level of antibody on the cell surface. Both coverslips were stained with Alexa 568 goat anti-mouse antibody in the absence of detergent for 1 h at room temperature. To determine the total CD59/β1-integrin level, another coverslip was fixed and stained with anti–CD59/β1-integrin antibody and then Alexa 568 anti-mouse antibody in saponin-containing staining buffer. All coverslips were subjected to confocal microscopy and ImageJ analysis. The rate of CD59/β1-integrin recycling was presented as the percentage of total CD59/β1-integrin recycled to the PM.

For TfR recycling, HeLa cells were grown on 100-mm dishes, resuspended with cell stripper (Mediatech, Corning, NY), and then washed with PBS. The cells were first pulsed with Alexa 633 transferrin for 1 h at 37°C (pulse), followed by washes with PBS. Cells were then divided into two groups. One (group A) was fixed directly with 4% (vol/vol) paraformaldehyde in PBS for 10 min, and the other (group B) was washed three times and incubated in fresh medium for 30 min (chase) before fixation. The amount of transferrin internalized after the pulse (A), as well as that remaining in the cells after the chase (B), was measured by flow cytometry. The recycling rate of TfR is presented as the percentage of internalized transferrin remaining in the cell after a 30-min chase, which was calculated as B/A. For both measurements, the values from three independent experiments were normalized.

Tubular endosome regrowth assay

HeLa cells were incubated with 100 nM (wt/vol) CAY inhibitor cocktail (CAY10593 plus CAY10594) for 30 min at 37°C, and the inhibitor was then washed away with complete medium. The cells were incubated in fresh medium for 20 min or 1 h before fixation with 4% (vol/vol) paraformaldehyde. The coverslips were stained for MICAL-L1 to observe the loss and regrowth of TREs by confocal microscopy.

ACKNOWLEDGMENTS

This research is supported by National Institutes of Health Grants R01GM087455 and R01GM074876. Support for the UNMC Advanced Microscopy Core Facility was provided by the Nebraska Research Initiative, a Fred and Pamela Buffett Cancer Center Support Grant (P30CA036727), and an Institutional Development Award from the National Institute of General Medical Sciences of the National Institutes of Health (P30GM106397). The Zeiss Elyra PS.1 superresolution microscope that we used is a National Institutes of Health Shared Instrumentation Grant–funded instrument.

REFERENCES

Antonescu CN, Aguet F, Danuser G, Schmid SL (2011). Phosphatidylinositol-(4,5)-bisphosphate regulates clathrin-coated pit initiation, stabilization, and size. Mol Biol Cell 22, 2588–2600.

Cai B, Caplan S, Naslavsky N (2012). cPLA2alpha and EHD1 interact and regulate the vesiculation of cholesterol-rich GPI-anchored protein-containing endosomes. Mol Biol Cell 23, 1874–1888.

Cai B, Katafiasz D, Horejsi V, Naslavsky N (2011). Pre-sorting endosomal transport of the GPI-anchored protein, CD59, is regulated by EHD1. Traffic 12, 102–120.

Cai B, Xie S, Liu F, Simone LC, Caplan S, Qin X, Naslavsky N (2014). Rapid degradation of the complement regulator, CD59, by a novel inhibitor. J Biol Chem 289, 12109–12125.

Caplan S, Naslavsky N, Hartnell LM, Lodge R, Polishchuk RS, Donaldson JG, Bonifacino JS (2002). A tubular EHD1-containing compartment involved in the recycling of major histocompatibility complex class I molecules to the plasma membrane. EMBO J 21, 2557–2567.

Caswell P, Norman J (2008). Endocytic transport of integrins during cell migration and invasion. Trends Cell Biol 18, 257–263.

Chi RJ, Harrison MS, Burd CG (2015). Biogenesis of endosome-derived transport carriers. Cell Mol Life Sci 72, 3441–3455.

Choudhury A, Sharma DK, Marks DL, Pagano RE (2004). Elevated endosomal cholesterol levels in Niemann-Pick cells inhibit rab4 and perturb membrane recycling. Mol Biol Cell 15, 4500–4511.

Dai J, Li J, Bos E, Porcionatto M, Premont RT, Bourgoin S, Peters PJ, Hsu VW (2004). ACAP1 promotes endocytic recycling by recognizing recycling sorting signals. Dev Cell 7, 771–776.

Daro E, van der Sluijs P, Galli T, Mellman I (1996). Rab4 and cellubrevin define different early endosome populations on the pathway of transferrin receptor recycling. Proc Natl Acad Sci USA 93, 9559–9564.

Daumke O, Lundmark R, Vallis Y, Martens S, Butler PJ, McMahon HT (2007). Architectural and mechanistic insights into an EHD ATPase involved in membrane remodelling. Nature 449, 923–927.

Donaldson JG, Porat-Shliom N, Cohen LA (2009). Clathrin-independent endocytosis: a unique platform for cell signaling and PM remodeling. Cell Signal 21, 1–6.

Flesch FM, Voorhout WF, Colenbrander B, van Golde LM, Gadella BM (1998). Use of lectins to characterize plasma membrane preparations from boar spermatozoa: a novel technique for monitoring membrane purity and quantity. Biol Reprod 59, 1530–1539.

Giridharan SS, Cai B, Vitale N, Naslavsky N, Caplan S (2013). Cooperation of MICAL-L1, syndapin2, and phosphatidic acid in tubular recycling endosome biogenesis. Mol Biol Cell 24, S1–S151776–1790.

Grant BD, Donaldson JG (2009). Pathways and mechanisms of endocytic recycling. Nat Rev Mol Cell Biol 10, 597–608.

Hales CM, Vaerman JP, Goldenring JR (2002). Rab11 family interacting protein 2 associates with Myosin Vb and regulates plasma membrane recycling. J Biol Chem 277, 50415–50421.

Hattula K, Furuhjelm J, Tikkanen J, Tanhuanpaa K, Laakkonen P, Peranen J (2006). Characterization of the Rab8-specific membrane traffic route linked to protrusion formation. J Cell Sci 119, 4866–4877.

Hehnly H, Chen CT, Powers CM, Liu HL, Doxsey S (2012). The centrosome regulates the Rab11- dependent recycling endosome pathway at appendages of the mother centriole. Curr Biol 22, 1944–1950.

Hopkins CR (1983). Intracellular routing of transferrin and transferrin receptors in epidermoid carcinoma A431 cells. Cell 35, 321–330.

Jovic M, Naslavsky N, Rapaport D, Horowitz M, Caplan S (2007). EHD1 regulates beta1 integrin endosomal transport: effects on focal adhesions, cell spreading and migration. J Cell Sci 120, 802–814.

Jovic M, Sharma M, Rahajeng J, Caplan S (2010). The early endosome: a busy sorting station for proteins at the crossroads. Histol Histopathol 25, 99–112.
Kirchhausen T, Owen D, Harrison SC (2014). Molecular structure, function, and dynamics of clathrin-mediated membrane traffic. Cold Spring Harb Perspect Biol 6, a016725.
Lapierre LA, Kumar R, Hales CM, Navarre J, Bhartur SG, Burnette JO, Provance DW Jr, Mercer JA, Bahler M, Goldenring JR (2001). Myosin vb is associated with plasma membrane recycling systems. Mol Biol Cell 12, 1843–1857.
Magadan JG, Barbieri MA, Mesa R, Stahl PD, Mayorga LS (2006). Rab22a regulates the sorting of transferrin to recycling endosomes. Mol Cell Biol 26, 2595–2614.
Maldonado-Baez L, Williamson C, Donaldson JG (2013). Clathrin-independent endocytosis: a cargo-centric view. Exp Cell Res 319, 2759–2769.
Marsh EW, Leopold PL, Jones NL, Maxfield FR (1995). Oligomerized transferrin receptors are selectively retained by a lumenal sorting signal in a long-lived endocytic recycling compartment. J Cell Biol 129, 1509–1522.
Maxfield FR, McGraw TE (2004). Endocytic recycling. Nat Rev Mol Cell Biol 5, 121–132.
Mayor S, Parton RG, Donaldson JG (2014). Clathrin-independent pathways of endocytosis. Cold Spring Harb Perspect Biol 6, a016758.
Mayor S, Presley JF, Maxfield FR (1993). Sorting of membrane components from endosomes and subsequent recycling to the cell surface occurs by a bulk flow process. J Cell Biol 121, 1257–1269.
Montagnac G, Echard A, Chavrier P (2008). Endocytic traffic in animal cell cytokinesis. Curr Opin Cell Biol 20, 454–461.
Naslavsky N, Caplan S (2011). EHD proteins: key conductors of endocytic transport. Trends Cell Biol 21, 122–131.
Naslavsky N, Weigert R, Donaldson JG (2003). Convergence of non-clathrin- and clathrin-derived endosomes involves Arf6 inactivation and changes in phosphoinositides. Mol Biol Cell 14, 417–431.
Ovesny M, Krizek P, Borkovec J, Svindrych Z, Hagen GM (2014). ThunderSTORM: a comprehensive ImageJ plug-in for PALM and STORM data analysis and super-resolution imaging. Bioinformatics 30, 2389–2390.
Powelka AM, Sun J, Li J, Gao M, Shaw LM, Sonnenberg A, Hsu VW (2004). Stimulation-dependent recycling of integrin beta1 regulated by ARF6 and Rab11. Traffic 5, 20–36.
Radhakrishna H, Donaldson JG (1997). ADP-ribosylation factor 6 regulates a novel plasma membrane recycling pathway. J Cell Biol 139, 49–61.
Rahajeng J, Giridharan SS, Naslavsky N, Caplan S (2010). Collapsin response mediator protein-2 (Crmp2) regulates trafficking by linking endocytic regulatory proteins to dynein motors. J Biol Chem 285, 31918–31922.
Reinecke JB, Katafiasz D, Naslavsky N, Caplan S (2015). Novel functions for the endocytic regulatory proteins MICAL-L1 and EHD1 in mitosis. Traffic 16, 48–67.
Ren M, Xu G, Zeng J, De Lemos-Chiarandini C, Adesnik M, Sabatini DD (1998). Hydrolysis of GTP on rab11 is required for the direct delivery of transferrin from the pericentriolar recycling compartment to the cell surface but not from sorting endosomes. Proc Natl Acad Sci USA 95, 6187–6192.
Sandvig K, Torgersen ML, Raa HA, van Deurs B (2008). Clathrin-independent endocytosis: from nonexisting to an extreme degree of complexity. Histochem Cell Biol 129, 267–276.
Sharma M, Giridharan SS, Rahajeng J, Naslavsky N, Caplan S (2009). MICAL-L1 links EHD1 to tubular recycling endosomes and regulates receptor recycling. Mol Biol Cell 20, 5181–5194.
Skop AR, Bergmann D, Mohler WA, White JG (2001). Completion of cytokinesis in C. elegans requires a brefeldin A-sensitive membrane accumulation at the cleavage furrow apex. Curr Biol 11, 735–746.
Sonnichsen B, De Renzis S, Nielsen E, Rietdorf J, Zerial M (2000). Distinct membrane domains on endosomes in the recycling pathway visualized by multicolor imaging of Rab4, Rab5, and Rab11. J Cell Biol 149, 901–914.
van der Sluijs P, Hull M, Webster P, Male P, Goud B, Mellman I (1992). The small GTP-binding protein rab4 controls an early sorting event on the endocytic pathway. Cell 70, 729–740.
Wang E, Brown PS, Aroeti B, Chapin SJ, Mostov KE, Dunn KW (2000). Apical and basolateral endocytic pathways of MDCK cells meet in acidic common endosomes distinct from a nearly-neutral apical recycling endosome. Traffic 1, 480–493.
Weigert R, Yeung AC, Li J, Donaldson JG (2004). Rab22a regulates the recycling of membrane proteins internalized independently of clathrin. Mol Biol Cell 15, 3758–3770.
Xie S, Naslavsky N, Caplan S (2014). Diacylglycerol kinase alpha regulates tubular recycling endosome biogenesis and major histocompatibility complex class I recycling. J Biol Chem 289, 31914–26.
Yamashiro DJ, Tycko B, Fluss SR, Maxfield FR (1984). Segregation of transferrin to a mildly acidic (pH 6.5) para-Golgi compartment in the recycling pathway. Cell 37, 789–800.